Acta Oceanol. Sin., 2024, Vol. 43, No. 12, P. 123–140
https://doi.org/10.1007/s13131-024-2386-8
http://www.aosocean.com
E-mail: ocean2@hyxb.org.cn

SAR-based oil spill detection and impact assessment on coastal and marine environments

Muhammad Ozair[1], Muhammad Farooq Iqbal[1]*, Irfan Mahmood[1], Saima Naz[1]

[1] Applied Geo-Informatics Research Lab, Department of Meteorology, COMSATS University Islamabad, Islamabad 45550, Pakistan

Received 15 December 2023; accepted 24 July 2024

Abstract

The proposed study focuses on the reported oil spill detection and assessments of oil impacts on marine ecosystems. Five selected oil spills, including those in East China Sea, Balikpapan Bay, Red Sea, Mauritius coast, and Colombo coast were detected using the Sentinel-1 satellite dataset. Sentinel-2/Landsat 8, and Sentinel-5 Precursor (S-5P) satellite datasets were utilized to observe the impacts of oil spills on vegetation cover and air quality respectively. Synthetic aperture radar-based oil spill detection techniques are effective in monitoring oil pollution. Impacts of oil spills on vegetation are monitored via different vegetation indices. The East China Sea spill moved around 190 km from the source point. The area of vegetation cover impacted by the Balikpapan Bay oil spill was 118 km^2. Near real-time data of different toxic gases from S-5P were analyzed for Sri Lanka and the Red Sea using the Google Earth Engine. It is concluded that wind speed was between the range of 3 m/s to 9 m/s that is favorable for the oil spill detection, and it is also observed that wind direction had impacts on oil spill movement as well. Vegetation Indices provide highly reliable results for the four events but the Red Sea oil spill findings were not satisfactory due to low vegetation cover in this area.

Key words: oil spill detection, vegetation cover, air quality assessment, sentinel, Synthetic Aperture Radar (SAR)

Citation: Ozair Muhammad, Iqbal Muhammad Farooq, Mahmood Irfan, Naz Saima. 2024. SAR-based oil spill detection and impact assessment on coastal and marine environments. Acta Oceanologica Sinica, 43(12): 123–140, doi: 10.1007/s13131-024-2386-8

1 Introduction

Oil spills have become more common in recent years due to increased oil extraction and shipping, driven by rising global demand (Yekeen et al., 2020). Approximately 45% of global oil spills are triggered by anthropogenic activities, such as discharge from oil tankers, cleaning of oil tankers and oil extraction (Alaa El-Din et al., 2018). Oil transportation accounts for 5% of sea oil pollution globally (Lu, 2003). Extensive oil spillage on coastlines has significant effects on marine organisms and the environment (Peterson et al., 2003a, b). Oil has a persistent nature and degrades slowly; mineral oil creates layers on the sea surface and stays there for a long period (Chiu et al., 2018). Oil restricts sunlight penetration into the deep ocean, diminishing photosynthetic activity in aquatic plants.

Oil spills pose a serious risk to marine vegetation and burning oil releases numerous gaseous pollutants into the atmosphere. The risk of oil spills is enhanced when the disaster response teams are unable to correctly assess the source of the leakage (Fan et al., 2015). Previously, conventional *in-situ* monitoring methods were selected for detecting spills. However, this technique came with its own set of concerns, starting from close interaction with oil to other site risks (Fan et al., 2015). Later, jets and coastguard services were launched as part of ocean monitoring systems. Despite its reliability, the significant expense of mapping, massive areas have restricted its utilization (Brekke and Solberg, 2005). From a few years, Remote Sensing (RS) methods seem to be more reliable, especially because they may be used at any time (Skrunes et al., 2014; Alpers et al., 2017; Naz et al., 2021). Both active and passive techniques are widely used for oil spill detection mapping and differentiating between various oil types. Passive RS uses different ranges of spectral bands like the visible, infrared, and thermal infrared portion of the electromagnetic spectrum (Zhao et al., 2015). The shadow, high clouds, and sun glint are three main barriers to the usage of passive RS (Drusch et al., 2012). The Synthetic Aperture Radar (SAR) systems are often used in conjunction with the existing ground-based observing systems, ships, and jets to provide comprehensive coverage of oceanic surfaces. The SAR technology provides large spatial coverage, day/night and all-weather data (Fiscella et al., 2000; Alpers et al., 2017).

Naz et al. (2021) suggested the utilization of geospatial techniques in combination with RS for better assessment and mapping of oil spills and their trajectories. Oil spills creates a smooth surface over the surface of ocean as a result the ocean waves dampens and because of this smooth surface low backscatter returns and area appears as a dark patch over the water surface (Brekke and Solberg, 2005; Marghany and Van Genderen, 2014). However, other similar patterns, created by some other sources like high/low winds or currents, rain cells and other meteorological phenomena also create oil spill-like dark paths called look-alikes (Brekke and Solberg, 2005). Oil spill detection can be achieved using four steps: (1) dark region identification, (2) extraction of features, (3) oil/look-alikes discrimination and (4) classification. Vertical-Vertical (VV) polarization is very effective for the detection of dark areas over the surface of ocean and VV polarization enables greater differentiation of oil from other look-alikes than Horizontal-Horizontal (HH) polarization (Migliaccio et al., 2015).

*Corresponding author, E-mail: farooqbuzdar@gmail.com

Monitoring the routes and movement of ships that are carrying oil spills enables the researchers and environmental authorities to identify high risk areas and develop quick response plans. Effective response strategies can be utilized to control and clean up oil spills by minimizing harm to the coastal vegetation and fauna. An oil spill in the regional ecosystem might put pressure on the natural vegetation in the area (Freedman, 1995; Li et al., 2005). Approximately 10 000 oil spills incidents were reported in the Niger Delta of Nigeria (NDN) for the period from 1970 to 2018. Around thirteen million barrels of oil spillage have impacted the coastal forest area. The devastating environmental impact occurred in the NDN due to spillages of petroleum products that lead to the destruction of natural mangrove forests (Chiu et al., 2018). Changes in plant spectral reflectance might be linked to oil pollution stress (Noomen and Skidmore, 2009). Oil spills severely impact coastal vegetation and wetlands located in the marine ecosystem's intertidal zone. Extended exposure to oil can smother and poison plants, altering soil chemistry. In the past 60 years, over 238 major oil spills have affected around 1.94×10^6 hm^2 (1 hm^2 = 10^4 m^2) of these habitats, releasing over 5.5×10^6 t of oil (Jana et al., 2016).

Traditional techniques of examining environmental contamination or pollution are costly and time-consuming, hence RS provides an effective, efficient, economical, and non-invasive method for detecting damage to flora caused by oil slicks. The effects on plants due to oil spills have been identified using several RS approaches. Spectral indicators can be used to examine the relationship between plant life and oil contamination (Arellano et al., 2015). Researchers used data from the Airborne Visible/Infrared Imaging Spectrometer (AVIRIS) to determine plant stress and recovery rate after oil spillage in marshland regions of Louisiana, USA, through Normalized Difference Vegetation Index (NDVI) techniques (Khanna et al., 2013). A visible smoke plume of soot and other combustion products is usually produced by burning oil spills. This emits plenty of hazardous pollutants into the coastal atmosphere, including CO, NO_2, SO_2, and a variety of organic contaminants (Evans et al., 2001).

The goal of the current study is to detect oil spills in different locations and check the movement of oil spills in next few days using active RS techniques and to evaluate the impact of oil spills on vegetation using different indices such as NDVI, Enhanced Vegetation Index (EVI), Leaf Chlorophyll Index (LCI), and Normalized Difference Water Index (NDWI) from passive RS techniques. Furthermore, monitoring of gaseous pollutants including CO, NO_2, and SO_2 was also assessed due to burning oil spills. Oil pollution is very harmful for the fragile marine ecosystem. Near real-time (NRT) mapping and assessment of impacts can save the economy and biodiversity loss at coastal areas. Impact assessment of oil spill on vegetation and air quality is novelty of the proposed work, that will surely help cleaning operations at the risk sites and mitigate the bad impacts up to some extent. This paper is organized as follows. Section 2 contains details of the study area, whereas datasets and methodology are presented in Section 3. The results are explained in Section 4. Results are discussed in Section 5, whereas conclusions are summarized in Section 6.

2 Study area

Figure 1 displays the geographic locations of selected oil spill events including Sanchi (East China Sea), Balikpapan (Java Sea), Jeddah (Red Sea), Wakashio and Sri Lanka oil spills (Indian Ocean). Sanchi oil tanker loaded with 111 000 t of condensate, an ultra-light, highly flammable crude oil collided with CF Crystal, a cargo ship from Hong Kong in the East China Sea on 6 January 2018. On 14 January 2018, eight days after the accident, the oil tanker sank roughly 151 nautical miles away from the accident site (Yin et al., 2018; Zhang et al., 2020). Sanchi sank carrying about 1 900 t of petroleum oil (bunker oil). As a result, the accident created four oil slicks covering a total area of 100 km^2 and the oil spill even reached the southern islands of Japan (Yin et al., 2018).

The Balikpapan Bay oil spill was Indonesia's worst ocean pollution catastrophe. It was reported on 29 March 2018, due to Pertamina underwater pipeline rupture. Satellite data of 2 April 2018, taken from the National Institute of Aeronautics and Space (NIAS) showed that the spill spread around 129.87 km^2 in the Ba-

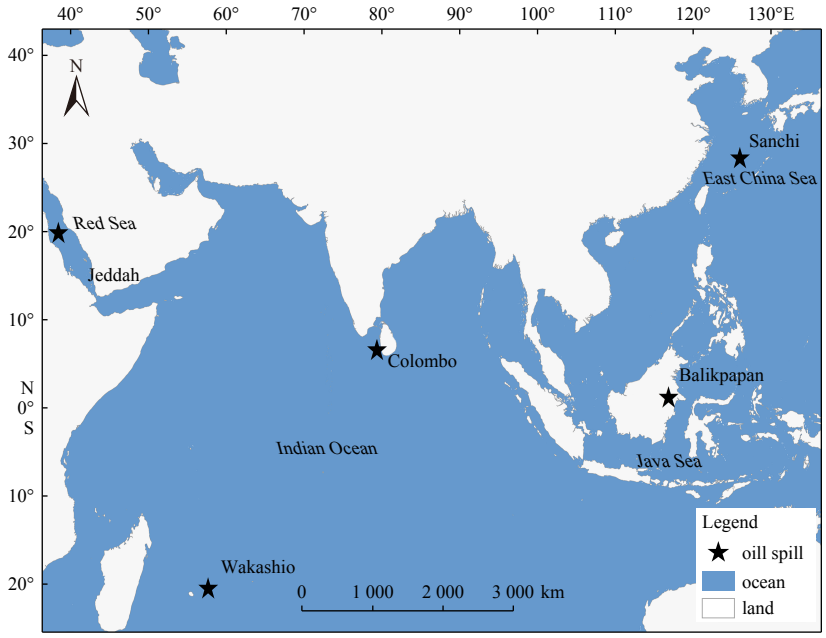

Fig. 1. Study area map showing oil spillage incident locations.

likpapan Bay due to waves and currents. Around 0.34 km^2 of mangrove-covered area in the village of Kariangau, and some other 6 000 mangrove plants along with 2 000 mangrove plant seeds in the village of Atas Air Margasari, were impacted because of spillage (Nur et al., 2018; Prastyani and Basith, 2018).

The Jeddah oil spill incident took place on 11 October 2019 in the Red Sea approximately 95 km away from the coast of Jeddah, reaching the coastal land within a week. The spill posed a severe threat to the biodiversity and fisheries of the Red Sea as well as to international shipping routes (Nukapothula et al., 2021; Vankayalapati et al., 2023).

On August 6, 2020, an oil spill occurred when the 300 m long Wakashio Japanese bulk carrier ship hit the coral reef while moving from China to Brazil with 3 900 t of low-sulfur fuel oil and 200 t of diesel (Rajendran et al., 2021). This spill took place in an environmentally sensitive region with rare species protected by the *Ramsar Convention on Wetlands*, an international treaty aimed to preserve and sustain wetlands.

Sri Lanka oil spill occurred near the coast of Colombo on 6 June 2021, when the Singapore registered Xpress Pearl had been on fire for almost two weeks and released many pollutants into the atmosphere. The ship carried 350 t of bunker fuel oil. The cargo ship also contained many containers which were loaded with plastics and chemicals.

3 Data and methodology

3.1 *Datasets*

3.1.1 *Sentinel-1*

In this study, Sentinel-1 (S-1) satellite data was utilized for oil spill detection. The S-1 comprised two satellite collections including S-1A and S-1B. The S-1A was sent into space on 3 April 2014 whereas S-1B was sent on 25 April 2016 (Malenovský et al., 2012). The S-1 data consists of C-band radar imagery with a swath width of up to 250 km and resolution of 10 m × 10 m. The central frequency of S-1 is 5.40 GHz, corresponding to a wavelength of 5.55 cm and equipped with C-band. The C-band frequency ranges from 4 GHz to 8 GHz (Fingas and Brown, 2014; Fingas and Brown, 2018). Table 1 shows S-1 product characteristics. In the current study, Interferometric Wide (IW) swath mode was selected, which provides a wider spatial coverage of the earth's surface with a finer spatial resolution of 5 m × 20 m (Cantorna et al., 2019). This mode also allows to perform interferometric analysis and coherence estimation, which are useful for detecting oil slicks and their characteristics. The S-1 data is available in dual-polarization such as VV+HV and HH+HV. However, in this study, S-1 Ground Range Detected (GRD) images of VV polarization were employed for the detection of oil spills (Mahindapala, 2020). Currently, open-access S-1, SAR data is easily accessible through ESA's Copernicus Data Space Ecosystem (https://dataspace.copernicus.eu/).

3.1.2 *Sentinel-2*

The Sentinel-2 (S-2) satellite data was utilized for the monitoring of vegetation and chlorophyll index. The S-2 consists of two identical polar-orbiting satellites (S-2A and S-2B) orbiting in a similar orbit (Drusch et al., 2012). A multi-spectral instrument measures reflected light in 13 spectral bands with a swath width of 290 km and spatial resolution extending from 10 m to 60 m. The MultiSpectral Instrument (MSI) of S-2 comprises 3 red-edge channels, as well as visible and near-infrared wavelengths, which have been determined to be critical for vegetation monitoring. The S-2 data products are available at two processing levels, 1C and 2A. Level-1C product contains the Top of Atmospheric (ToA) reflectance whereas Level-2A records the Bottom of Atmosphere (BoA) reflectance and these are atmospherically corrected (Delegido et al., 2011; Clevers and Gitelson, 2013; Schlemmer et al., 2013). In this study, S-2 multispectral level-2A, BoA data was utilized for the mapping of vegetation cover and Land Use Land Cover (LULC) classification.

3.1.3 *Landsat-8*

Landsat-8 (L8) multispectral sensor carries 11 spectral bands including Coastal, Visible, Near-infrared (NIR), Short-Wave Infrared (SWIR), Panchromatic (Pan), Cirrus, and Thermal Infrared Sensor (TIRS). The data collected from the L8 satellite was utilized for LULC mapping and monitoring of vegetation cover. The L8 satellite provides more precise data with a resolution of up to 30 m in various bands and has a temporal frequency of L8 is 16 d. In this study, L8 data was utilized for only two events to monitor the vegetation cover because S-2A was not available for that period (Ganjirad and Bagheri, 2024).

3.1.4 *Sentinel-5 Precursor*

The Sentinel-5 Precursor (S-5P) data was utilized to monitor the air quality after the burning of oil (Veefkind et al., 2012). The satellite is loaded with the highly sophisticated Tropospheric Monitoring Instrument (TROPOMI) device for determining ultraviolet-visible (270–500 nm), NIR (675–775 nm), and SWIR (2 305–2 385 nm) spectral channels, permitting it to gather data like NO_2, O_3, Formaldehyde, SO_2, CH_4 and CO with greater accuracy than ever before (Ewing et al., 2012; Zheng et al., 2019). The TROPOMI offers a large spatial resolution of 7 km × 3.5 km and cloud-free observations per day (Guanter et al., 2015). In this study, S-5P satellite data (<10% cloud cover) before and after the event was used.

3.1.5 *Wind data*

The SAR based ocean surface wind speed data was derived from Geophysical Model Functions (GMFs) VV-polarization of S-1 satellite data freely available (https://dataspace.copernicus.

Table 1. Sentinel-1 operational product characteristics [Interferometric Wide Swath (IW), Strip Map (SM), Extended Interferometric Wide Swath (EW), Azimuth (Az), Full Resolution (FR), High Resolution (HR), Medium Resolution (MR), and Range (Rz)]

Data mode	Resolution class	Resolution (Rz × Az)/m^2	Pixel spacing (Rz × Az)/m^2	Number of looks (Rz × Az)	Swath/km
SM	FR	9 × 9	4 × 4	2 × 2	80
SM	HR	23 × 23	10 × 10	6 × 6	80
SM	MR	84 × 84	40 × 40	22 × 22	80
IW	HR	20 × 22	10 × 10	5 × 1	250
IW	MR	88 × 89	40 × 40	22 × 5	250
EW	HR	50 × 50	25 × 25	3 × 1	400
EW	MR	93 × 87	40 × 40	6 × 2	400

eu/) . Wind speeds are derived from the Normalized Radar Cross Section (NRCS) and image geometry of the calibrated SAR images, together with the local SAR retrieved wind direction.

3.2 *Methods*

3.2.1 *Oil spill detection*

Three images of S-1, GRD product for each incident were obtained and analyzed based on data accessibility. The image acquisition sequence was (1) before the event, (2) immediately after the event, and (3) late post-event images (to analyze the movement of oil spills). Table 2 shows the details of each event including location, coordinates, type, and volume of spilled oil. The oil spill detection was carried out using the steps were (1) image preprocessing, (2) detection of dark areas, (3) parameter extraction and (4) image classification.

Image preprocessing includes image subset, radiometric calibration, multi-look speckle filtering, ellipsoid correction, and land/sea masking. Area of Interest (AOI) was selected by the image subset technique (Mdakane and Kleynhans, 2022). Calibration was done to get pixel values representing the radar backscatter. The S-1 images were calibrated to reduce incidence angle differences (Mera et al., 2012). SAR imagery has "salt and paper" noise called speckle noise. The Lee Sigma filter (7 × 7 kernel size and 3 × 3 window) was applied to remove this noise (Cervantes-Hernández et al., 2024). The Lee Sigma filter is dependent on two sigma Gaussian distribution probability and integrates the speckle multiplicative noise model as described in Eq. (1).

$$z(k,l) = x(k,l) \times v(k,l), \tag{1}$$

where $z(k, l)$ is the pixel of (k, l)-th in the amplitude of a SAR image, $x(k, l)$ is the image reflection and $v(k, l)$ denotes the speckle noise (Lee et al., 2008).

Multi-looking is a technique that is quite effective in processing the geometry of a complex image. The range look was selected as 1, azimuth look as 2, whereas the mean ground range square pixel was selected as 5.39. Ellipsoid correction compensates for the distance distortions and aligns the image with the real-world location. In this study, Geolocation Grid (GG) was applied to correct the images geometrically (Misra and Balaji, 2017). Since our focus was sea surface area, therefore the "Mask Out Land" technique was applied to avoid the processing of land areas. This operation replaces all land pixels with the null values and decreases the image size.

A binary classification method based on pixel values was used to identify dark patches. High contrast in SAR images was achieved using VV polarization, providing a significant difference between oil spills and clean ocean water (Lu, 2003). According to "Bragg Scattering Theory" the NRCS (σ^0) incidence angle between 20° and 70° is proportional to the spectral energy density of the Bragg waves $E(\pm k_B)$ and is described in Eq. (2).

$$\sigma^0 = C_{ij}(\varepsilon, \vartheta)[E(+k_B) + E(-k_B)]. \tag{2}$$

where the $C_{ij}(\varepsilon, \vartheta)$ Bragg coefficient is dependent on the incident angle. In which (i, j = Horizontal/Vertical polarization) is expressing backscattered polarization of waves and ε is the dielectric constant of seawater. E is the spectral energy of waves and k_B is Bragg wave number (Lu, 2003) as described in Eq. (3).

$$K_B = \frac{4\pi \sin\vartheta}{\lambda_o}. \tag{3}$$

The wavelength of radar is denoted by λ, Bragg wavelength λ_B is described in Eq. (4).

$$\lambda_B = \frac{\lambda_0}{2\sin\vartheta} \tag{4}$$

The dumping ratio $\Delta\sigma(K_B)$ is defined as the ratio of the radar back-scattered power from the clean and oil-covered sea surface (Lu, 2003) as described in Eq. (5).

$$\Delta\sigma(K_B) = \frac{E_{sea}(+K_B) + E_{sea}(-K_B)}{2E_{oil}(+K_B) + E_{oil}(-K_B)}, \tag{5}$$

where E is the spectral energy of waves, E_{sea} denotes clear sea surface and E_{oil} denotes oil covered sea surface.

Logarithmic ratio of pre and post image formation has been applied for visibility enhancement of oil spill features (Ajadi et al., 2018), as described in Eq. (6).

$$X_{LS} = 10\lg(x) + 10\lg\left(\frac{X_i(i,j)}{X_R(i,j)}\right), \tag{6}$$

where X_{LS} is the image ratio, x is contribution of an additive noise, X_R is pre-event oil spill image and X_i is post-event image.

In this study adaptive thresholding technique is used for dark area detection. This algorithm identifies dark pixels through a trained operator which goes through the image and identifies the pixels with low intensity values and separates dark patches from the clean ocean surface (Misra and Balaji, 2017). The number of iterations were 20 and threshold shift was set according to the difference of image intensity values because it is observed that oil spills are darkest in colour and have lowest intensity. Threshold values for the East China Sea oil spill was set as <–2.5 dB, for Balikpapan Bay oil spill was set as <–5 dB, for Red Sea oil spill was set as <–4.5 dB, for Mauritius coast oil spill was set as <–2 dB and

Table 2. Geographic location and oil type of spill events

No.	Location	Latitude	Longitude	Event date	Pre-acquisition date	Post-acquisition date	Oil spill volume/t	Type of oil
1	East China Sea	28.634°N	125.617°E	6 January 2018	27 December 2017	20 January 2018	111 000/1 900	Ultra-Light Highly Flammable Crude Oil (ULHFCO)/ Bunker Oil (BO)
2	Balikpapan Bay (Indonesia)	1.830°N	116.507°E	29 March 2018	8 March 2018	1 April 2018	–	Crude Oil (CO)
3	Red Sea (Jeddah)	20.447°N	38.339°E	11 October 2019	1 September 2019	13 October 2019	–	CO
4	Mauritius coast	20.221°S	57.617°E	6 August 2020	17 July 2020	10 August 2020	4 100	Low Sulfur Fuel (LSF)
5	Colombo (Sri Lanka)	6.847°N	79.271°E	26 May 2021	3 May 2021	8 June 2021	350	BO

Note: – represents no data.

for Sri Lanka oil spill event was set as <–1.5 dB.

In the parameter's extraction stage, feature's properties of the detected dark areas are calculated from the area of interest. Segmented and detected parts of the image are further processed to extract parameters as it is a prerequisite for image classification (Mera et al., 2012). Proposed NRT contains two main classes including geometric and backscatter parameters. These classes have proven well for the NRT oil spill detection algorithm (Topouzelis and Singha, 2017). Geometric parameters include dark object area, perimeter (length) and object complexity are described in Eq. (7).

$$C = \frac{P}{2\sqrt{\pi A}}, \tag{7}$$

where C represents the complexity of an object (will take small value for simple geometry and large value for complex geometry). A denotes the area and P denotes perimeter of the dark object. Oil spill spreading factor is computed in Eq. (8).

$$S = \frac{100\lambda_2}{\lambda_1 + \lambda_2}. \tag{8}$$

where S represents the spreading parameter that is derived from principal component analysis, λ_1 and λ_2 are the eigenvalues associated with the covariance matrix.

In image classification, dark objects are classified as oil spills. Vector information of parameter is used in classification stage to separate oil spill from look-alikes (Shu et al., 2010; Migliaccio et al., 2015; Misra and Balaji, 2017; Topouzelis and Singha, 2017). In this study, K-means clustering algorithm (described in Eq. (9)) is used for the clustering of dark patches for the separation of oil spill from the look-alikes. K-means clustering is an unsupervised classification technique (Zalik, 2008) and assumes that cluster numbers are known and divides the dataset into fixed numbers.

$$C_i = \frac{1}{|C_i|} \sum_{x_t \in c_i} x_t, \tag{9}$$

where c_i is the mass point of all points in cluster C_i and x_t is a randomly picked point from input datasets (Zalik, 2008).

3.2.2 *Impact assessment of oil spill on vegetation*

In response to petroleum product contamination, the colour of the plant's leaves stem and trunk changes because of the loss of photosynthetic pigments. When oil spills occur near the coastal area, the daily tidal waves push the oil ashore, which results in oil deposits on the plant roots. There are 0–15 d, 15–30 d, 30 d to 1 a and 1–5 a stages of oil impact the vegetation to death of aquatic life, chlorosis and death of medium plants, death of and defoliation >5 m mangroves and death of and defoliation >10 m mangroves respectively. The oil sediments adhere to the root surface and become the main cause of chronic effects on the coastal vegetation (Ozigis et al., 2020). Timely detection of oil spills over forest areas can reduce the impacts. In this study, different Vegetation Indices (VI) were computed using L-8 and S-2A satellite data to analyze the vegetation status in coastal areas of reported oil spills events (Adamu et al., 2018; Bhatnagar et al., 2020; Frampton et al., 2013). Before applying for any VI, a line was digitized for each event near the coastal areas using Google Earth Pro (GEP) to study the vegetation impacts over the coastal region for each event. Buffer technique was applied on the left side of the line to get the required AOI. Table 3 shows the information for all events regarding buffer size, and data acquisition before and after the events. For all reported events, satellite data with less than 10% of cloud cover was acquired.

3.2.2.1 *NDVI*

NDVI is widely used to monitor the growth and health of vegetation and to identify areas of stress or damage (Adamu et al., 2018). NDVI value ranges from –1.0 to +1.0, where values greater than 0.20 indicate sparse vegetation (grassland and shrubs) and dense vegetation (healthy crops or tropical forests). In this study, threshold values of 0.20 were applied to analyze effects of oil spills on sparse and dense vegetation cover (Peng et al., 2016, 2019). NDVI is computed using Eq. (10).

$$\mathrm{NDVI} = \frac{(\mathrm{NIR} - \mathrm{Red})}{(\mathrm{NIR} + \mathrm{Red})}, \tag{10}$$

where NIR represents Band8 and Red represents Band4 of the S-2 satellite image.

3.2.2.2 *EVI*

EVI is an advanced vegetation indicator which is calculated to improve vegetated area monitoring by removing the canopy background signal and reducing atmospheric disturbances. EVI responds better to canopy fluctuations and canopy type than NDVI, and it does not become as saturated as NDVI when viewing areas with very dense green vegetation. The value ranges from –1 to +1 and for healthy vegetation its values fluctuate from 0.2 to 0.8 (Somvanshi and Kumari, 2020). In this study, EVI was used to assess the impacts of oil spills on vegetation cover and EVI was computed using Eq. (11).

$$\mathrm{EVI} = 2.5 \times \frac{\mathrm{NIR} - \mathrm{Red}}{(\mathrm{NIR} + 6 \times \mathrm{Red} - 7.5 \times \mathrm{Blue}) + 1}, \tag{11}$$

where NIR, Red and Blue are Band8, Band4 and Band2 respectively. Numeric values 6 and 7.5 are the coefficient aerosol resist-

Table 3. Event parameters and data acquisition dates for oil spill analysis

No.	Effected coastal region	Event location	Buffer size/km	Pre-acquisition date	Post-acquisition date
1	Japan coast	East China Sea	40	5 May 2016	9 October 2018
				9 October 2017	9 October 2019
2	Balikpapan Bay	Balikpapan Bay	5	7 August 2016	31 August 2018
				31 August 2017	31 August 2019
3	Jeddah coast	Red Sea	20	23 March 2017	22 March 2020
				23 March 2018	22 March 2021
4	Mauritius coast	Mauritius coast	1	29 January 2018	28 January 2021
				29 January 2019	28 January 2022
5	Colombo coast	Colombo coast	15	17 November 2019	21 November 2021
				21 November 2020	26 November 2022

ance values which use the blue band to remove the aerosol influences in the red channel and 2.5 is the gain factor.

3.2.2.3 *Leaf Chlorophyll Index*

Leaf Chlorophyll Index (LCI) is used to accurately represent chlorophyll contents in leaves, with less sensitivity to scattering from the leaf surface and internal structural variability (Pu et al., 2008). LCI value ranges from –1 to +1 and computed using Eq. (12).

$$\mathrm{LCI} = \frac{(\mathrm{Band8} - \mathrm{Band5})}{(\mathrm{Band8} + \mathrm{Band4})}, \tag{12}$$

whereas Band4, Band8 and Band5 represent red, NIR, and vegetation red edges.

3.2.2.4 *NDWI*

The SWIR reflectance indicates the changes in both plant water content and mushy mesophyll shape in canopy plants. The NIR reflectance is influenced by inner structure and dry matter content of the leaf but not by moisture content. The combination of the IR and SWIR reduces the effects of changes in the leaf's interior structure and chlorophyll content, enhancing the reliability of estimating the plant's water potential (Ozigis et al., 2020). NDWI is effective for detecting changes in land cover due to drought, fire, or deforestation and computed using Eq. (13).

$$\mathrm{NDWI} = \frac{\mathrm{NIR} - \mathrm{SWIR}}{\mathrm{NIR} + \mathrm{SWIR}}. \tag{13}$$

3.2.3 *Impact assessment of oil spill on air quality*

Burning oil in the oceanic water emits many harmful pollutants like CO, NO_2, SO_2, and various organic pollutants into the coastal atmosphere. Due to unavailability of data, only two oil spill events including Sri Lanka and the Red Sea were selected for the monitoring of oil pollutants. S-5P satellite data was used to assess the concentration of the pollutants. S-5P data with <10% cloud cover was selected, and cloud masking technique was applied to remove the effects of clouds. In this study, the average concentration of CO, NO_2, and SO_2 was acquired using the Google Earth Engine (GEE).

The Red Sea oil spill occurred on 11 October 2019, 95 km off the coast of Jeddah, Saudi Arabia. Pre- and post-event satellite images were acquired for 11 September and 13 October 2019 respectively to monitor the air quality a month prior to the spill and a month after it. Image data of 13 October 2020 was acquired for further monitoring, whereas pre-event data was not available. A buffer of 100 km was applied around the spill region to get the area of interest. The grid matrix of the study area was created using the Fishnet tool. The oil spill event occurred on 6 June 2021 off the coast of Colombo, Sri Lanka. Pre- and post-event images were obtained for 8 June 2020, 8 May 2021, and 8 June 2021, respectively (Zheng et al., 2019).

3.2.4 *Wind speed and direction*

Detectability of oil slicks depends on the ocean surface wind speed. If the wind speed is too low (<3 m/s), the clean sea surface will not have sufficient roughness to contrast with oil films (Ajadi et al., 2018). On the other hand, if wind speed is too high (>12 m/s), oil slicks will be dispersed by the surface waves and disappear from the sea surface (Mera et al., 2012). In this study wind speed and direction of all the events were plotted via wind rose diagram.

4 Results

In this study, five oil spill incidents were analyzed using active and passive RS techniques. Apart from oil spill detection, the impacts of oil spills on vegetation cover and as well as on air quality were studied. The obtained findings were divided into the following sections.

4.1 *Detection of oil spill*

Adaptive thresholding and K-means clustering were used for feature extraction and identification of dark regions in the image. However, these methods struggled with false positives caused by look-alikes, requiring additional validation steps.

4.1.1 *East China Sea oil spill*

In this event, an oil slick of approximately 52 km^2 was reported. However, due to high wind speed, only a small area of an oil spill was detected. Figure 2a displays a pre-event image of S-1 data obtained on 27 December 2017, where nothing like an oil spill was observed. Figure 2b displays the post event image, acquired on 20 January 2018, where the dark patch of the oil spill is clearly visible after applying a threshold of less than –2.5 dB. However, the detection was hindered by high wind speeds, which dispersed the oil. Figure 2c displays the classified image of the oil spill.

4.1.2 *Balikpapan Bay (Indonesia)*

Figure 3a displays the pre-event image of the Balikpapan oil spill, obtained on 8 March 2018 about 21 d before the oil spill event. After performing all the preprocessing steps on the pre-event image, no oil spill was detected. Figure 3b displays the post-event image. The detection method was employed on the GRD product of S-1 data, where 4 648 × 4 587 pixels were analyzed, and an oil spill was successfully detected. The contrast between the oil spill and ocean water, which was 5 dB, so the threshold value of 5 dB was selected to segregate the oil spills from the clean ocean water. However, the presence of look-alikes such as algae blooms complicated the classification. Figure 3c displays the classified image of where the detected oil spill was located.

4.1.3 *Red Sea oil spill (Jeddah)*

Figure 4a displays the pre-event GRD product of S-1 that was obtained on 1 September 2019 of the Red Sea Jeddah oil spills. All the pre-processing steps were applied on the image and there was no indication of oil spill. An oil spill (approximately 1 300 km^2) occurred on 11 September 2019 over a large water surface. A total of 8 911 × 8 221 pixels were processed with a threshold value less than 4.5 dB to detect the spilled oil. A Lee Sigma filter with a window size of 7 × 7 was applied to remove the speckle noise. Figure 4b displays the post-oil spill image where the spilled oil was clearly visible over the SAR image. However, strong currents dispersed the oil, complicating detection. Figure 4c displays the classified image of the detected oil spill.

4.1.4 *Mauritius oil spill*

Figure 5 displays the Mauritius coast oil spill event. Figure 5a displays no oil spill in the pre-event image data acquired on 17 July 2020. A total of 501 × 352 pixels were processed to accomplish the purpose of oil spill detection. Figure 5b displays a post-event image that was acquired on 10 August 2020 around 2 d after the accident and an oil spill was visible in the image. The contrast between the background ocean water and oil spill was clear. So, the threshold shift was set as less than –3.5 dB. However, the

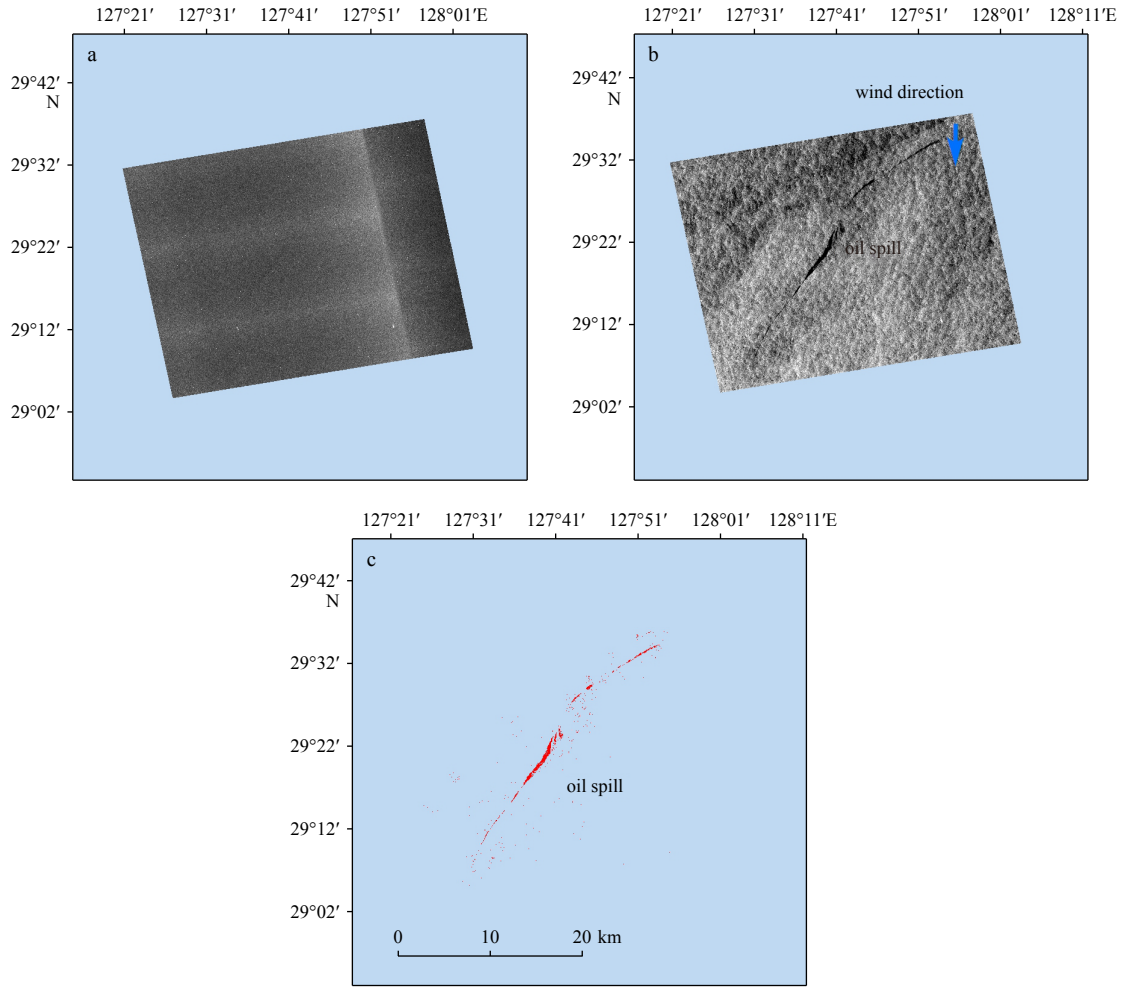

Fig. 2. East China Sea oil spill: a. pre-oil spill image (2017-12-27), b. post-oil spill image (2018-01-20), c. classified oil spill image (wind direction: south).

presence of ship wakes and natural slicks introduced noise into the classification. Figure 5c displays the classified image.

4.1.5 *Colombo oil spill (Sri Lanka)*

A total of 457 × 355 pixels were processed using the GRD product of S-1 data. Figure 6a displays a pre-event image that was acquired on 3 May 2021. The image is clear without any oil patch. Figure 6b displays the post-event image acquired two days after the event on 8th June 2021. A 1.5 dB adaptive threshold was applied to detect the oil spill. Figure 6c displays the classified image where oil spill is shown with purple color.

4.2 *Movement of oil spills*

As the oil spills into the oceans, it moves from the spill loca-

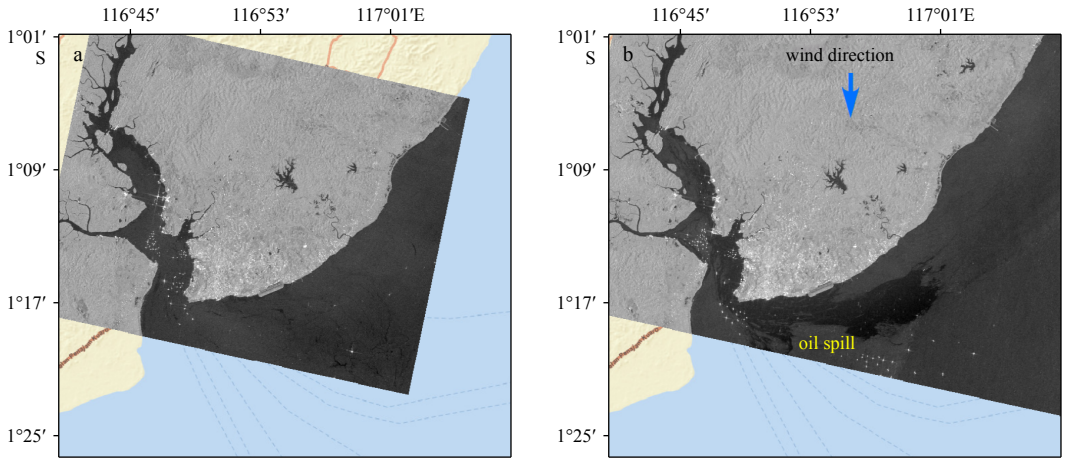

Fig. 3.

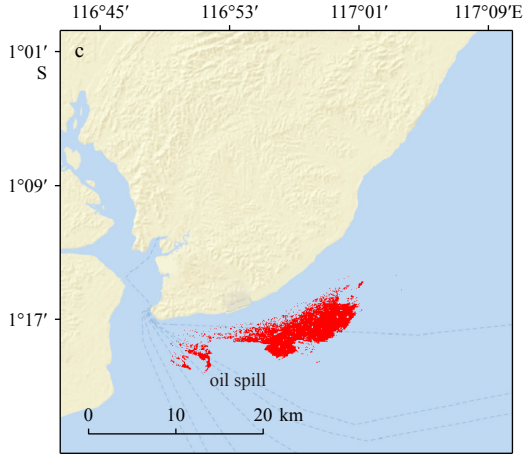

Fig. 3. Balikpapan oil spill: a. pre-oil spill image (2018-03-08), b. post-oil spill image (2018-04-01) with wind direction (blue arrow), c. classified oil spill image.

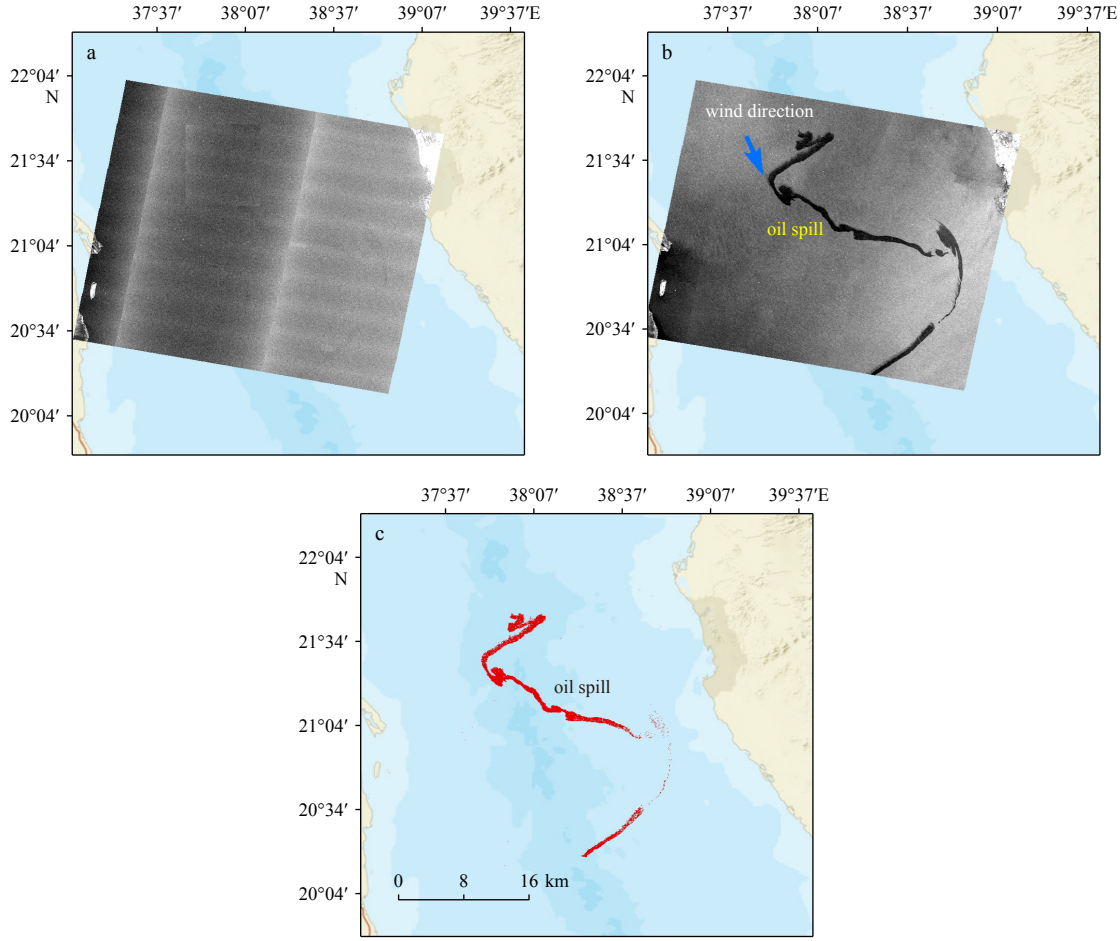

Fig. 4. Red Sea oil spill incident: a. pre-oil spill image (2019-09-01), b. post-oil spill image (2019-10-13) with wind direction (south), c. classified oil spill image.

tion to the nearby areas under the force of wind, wave, and currents. To analyze the impacts of oil spills for all the events late post images were processed. Figure 7 displays the oil movement of all studied events. Figure 7a displays the image of East China Sea acquired on 20 January 2018 where, 190 km oil spill movement from the source point was observed. However, Fig. 7b displays the movement of oil spill of Balikpapan Bay at different locations. In 13 d, oil moved around 25 km towards the coastal area. Figure 7c displays the map of Red Sea oil spill where the oil spill spread at large scale is observed because the rockets hit by the Iranian tanker and oil spill move along the tanker although extensive amounts of oil move towards the surrounding areas and approximately 97 km oil spill moved in 12 d. The Mauritius coast oil spills incident occurred in an environmentally sensitive region where oil spreads 9 km along the coast and adversely affected the natural vegetation as shown in Fig. 7d. Figure 7e displays the res-

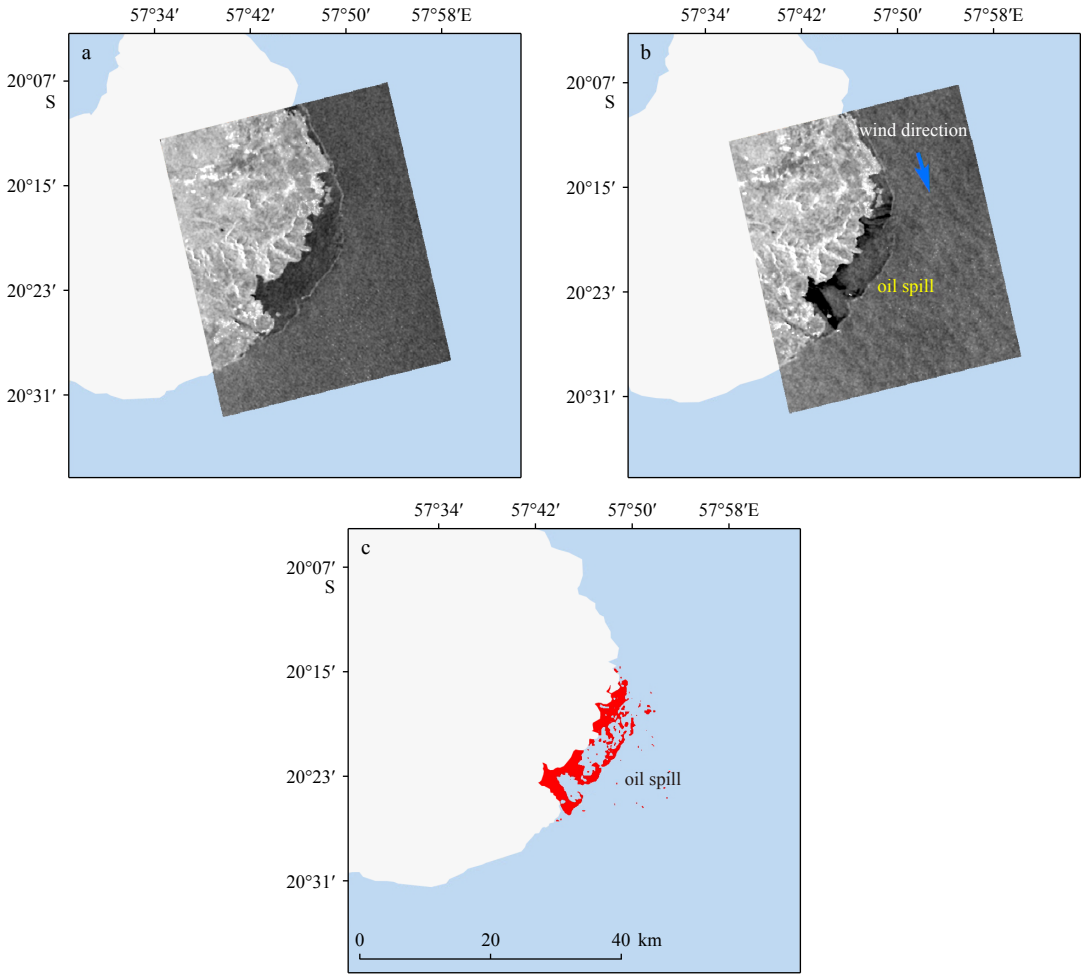

Fig. 5. Mauritius oil spill: a. pre-oil spill image (2020-07-17), b. post-oil spill image (2020-08-10) with wind direction (blue arrow), c. classified image.

ults of the oil spills movement towards the coast of Colombo. Most of the oil was burnt into the air and a considerable amount of oil was moved 8 km towards the coast.

4.3 *Wind speed and direction*

The wind rose diagram of each event was created to check the impacts of wind on oil spill movement. Figure 8 displays the wind speed and direction at the time of spill event. Figure 8a displays the wind rose diagram of the East China Sea oil spill event. Wind direction was observed towards the southern part of the image. However, wind speed around the spill was 3 m/s to 7 m/s, which is considered a favorable wind speed limit for accurate spill detection. Similarly, Fig. 8b shows the wind speed and direction of the Balikpapan Bay oil spill. Maximum wind flow is towards the south and low wind cells are found at the northeastern side of the event. Wind speed was between the range of 2 m/s to 7.5 m/s.

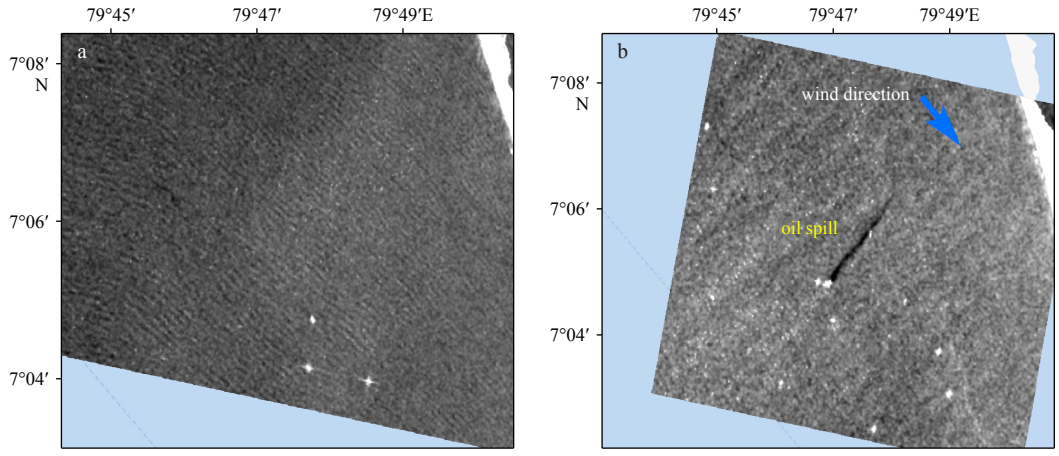

Fig. 6.

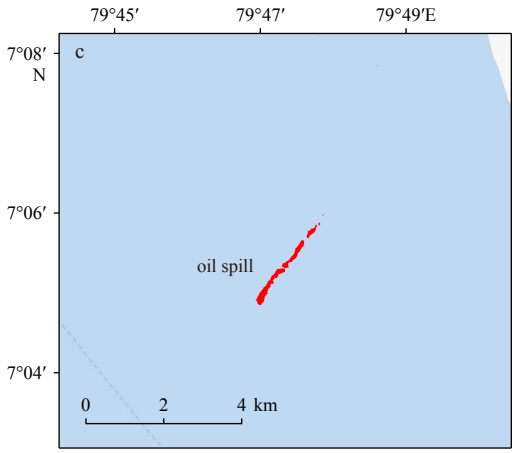

Fig. 6. Sri Lanka oil spill: a. pre-oil spill image (2021-05-03), b. post-oil spill image (2021-06-08) with wind direction and high wind cells, c. classified oil spill image with look-alike slick.

Figure 8c displays the minimum/maximum wind speed and direction of the Red Sea oil spill on 11 October 2019. Wind speed lies between 3.5 m/s and 8 m/s around the spill site and wind direction is observed towards the south and southeastern side. Figure 8d displays the wind speed and direction of the Mauritius coast oil spill. In this event high wind cells are also found at the time of the event. Minimum/maximum wind speed was observed 3 m/s to 9 m/s and direction was towards the south and northwestern side. Figure 8e displays the maximum and minimum wind speed of the Colombo oil spill. In this event, the wind direction is towards the southwestern side and high wind cells are shown at the western side. Wind speed was observed 3 m/s to 9 m/s.

4.4 *Impact assessment of oil spill on vegetation*

Vegetation indices results indicated that oil spills have a detrimental effect on vegetation cover. Oil spill's impact on vegetation can be classified as acute or chronic. Acute impacts range from chlorosis to plant death, and they are evident within the first two weeks following an oil spill. Chronic toxicity of oil leads to root abnormalities, altered growth rate, and structural changes after 1–5 a of exposure to oil.

4.4.1 *NDVI based assessment*

The impacts of the East China Sea oil spill on vegetation cover were assessed along the coastline of Japan from Kagoshima to Saikai. Figures 9a–d displays NDVI based assessment respect-

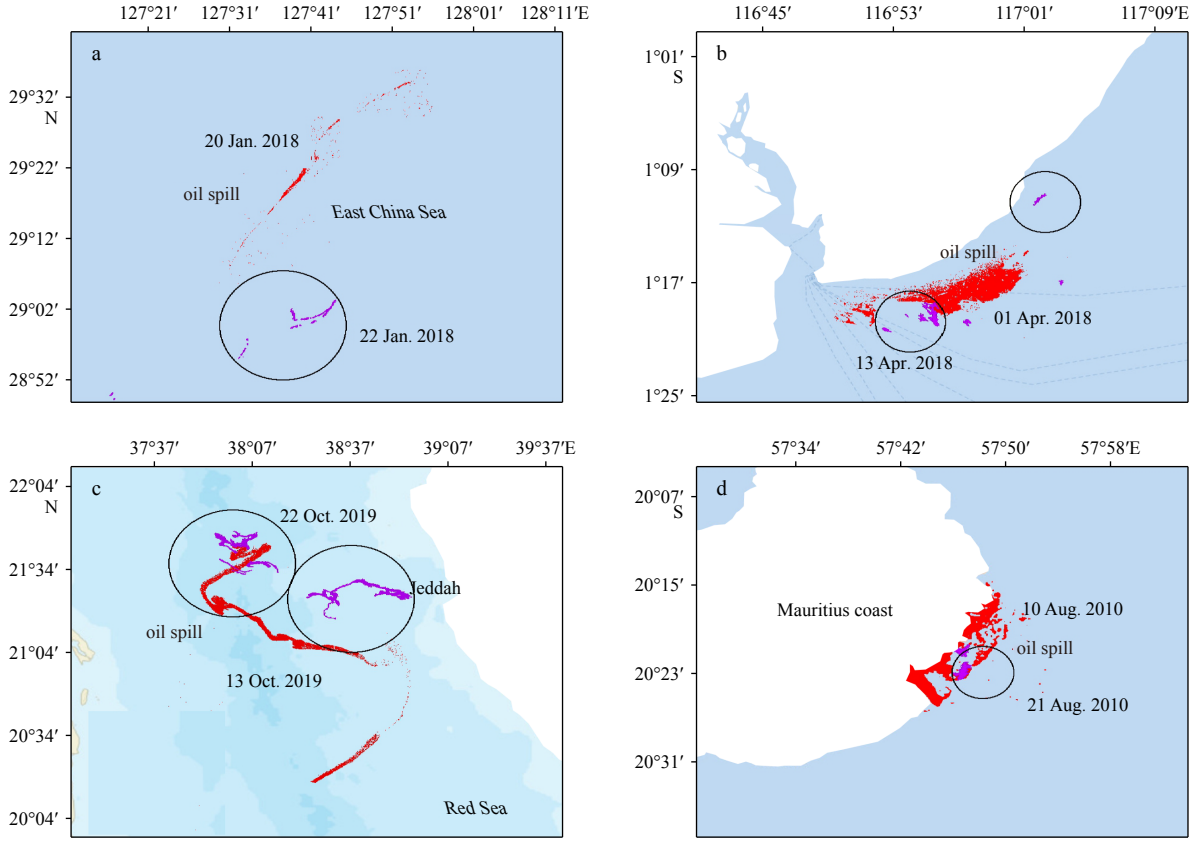

Fig. 7.

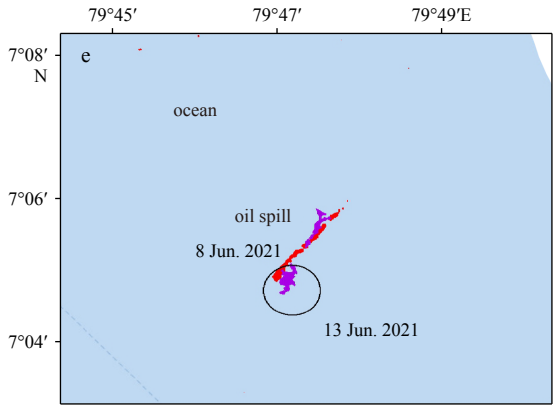

Fig. 7. Movement of oil spills over time: a. East China Sea (2018-01-22), b. Balikpapan Bay (2018-04-13), c. Red Sea (2019-10-25), d. Mauritius (2020-08-21), e. Sri Lanka (2021-06-13).

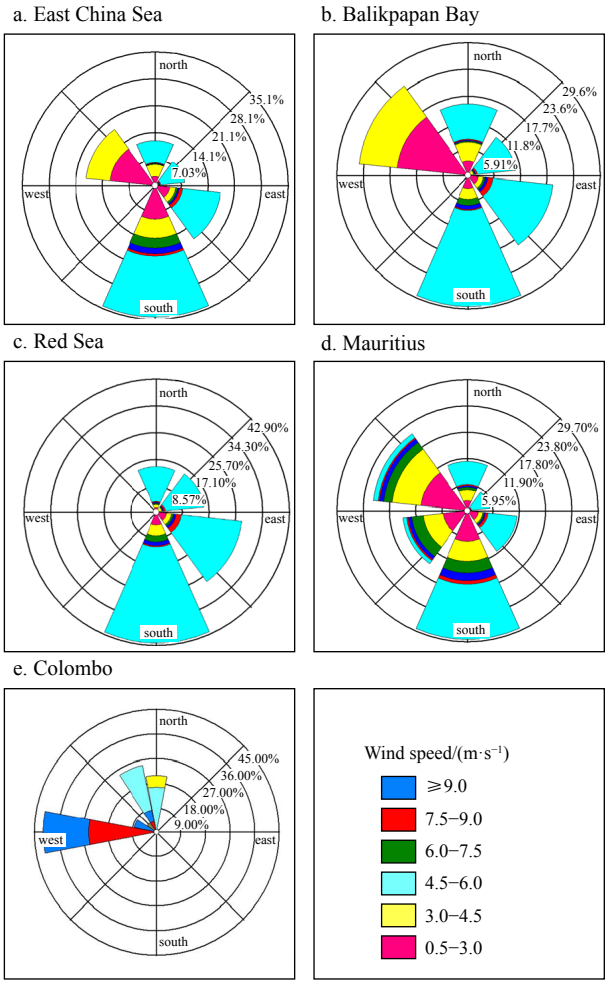

Fig. 8. Wind rose diagrams for oil spill event locations: a. East China Sea, b. Balikpapan Bay, c. Red Sea, d. Mauritius, and e. Colombo.

ively where the vegetation covered area decreased from 277 km² to 267 km². Figure 9e displays the NDVI results of Balikpapan Bay before the oil spill event on 5 May 2016, with a vegetation cover of 545 km². Figure 9f displays the vegetation covered area of 540 km² on 9 October 2017 whereas, Fig. 9g displays NDVI results after eight months of the event and the area of vegetation reduced to 510 km². Persistent nature and chronic toxicity of hydrocarbon pollution gradually deteriorated the root structure of the plants and caused mortality, resulting in a further reduction of vegetation cover to 487 km² as shown in Fig. 9h. Figures 9i–l displays no significant variations in vegetation cover due to low movements of waves and small area of vegetation on Jeddah coast.

Figures 9m and n displays the NDVI results of Mauritius Coast one and two years before the incident respectively. No abnormality was observed in the vegetation cover. However, one year after the event, the vegetation cover decreased 89 km² as shown in Fig. 9o, further reduction in vegetation covered area was observed after two years of oil spill as shown in Fig. 9p. The coastal area of Colombo consists of lagoons, salt marshes, beaches, and mangroves. Figure 9q displays the vegetation cover of 120 km² two years before the oil spill event. Figure 9r displays an increase of vegetation cover to 127 km² but after the five months of the oil spill there was an apparent decline in vegetation cover as shown in Fig. 9s. Vegetation covered area further decreases after the one year of the incident as shown on Fig. 9t.

4.4.2 *EVI based assessment*

EVI is an optimized index that is designed for the observation of vegetation and used simultaneously with NDVI to remove atmospheric influences. EVI was used to monitor the impacts of the East China Sea oil spill over the Japan coast. Figures 10a–d displays the results of EVI where 29 km² area of vegetation covered was reduced after the oil spill event. EVI findings of Balikpapan Bay show how the atmospheric influences affect the NDVI results. Figure 10e displays the vegetation covered area of 525 km² two years before the oil spill. In the years following the event, the vegetation cover decreased by 88 km² as shown in Figs 10g and h. EVI findings of the Jeddah coast are shown in Fig. 10i.

4.4.3 *LCI based assessment*

Figures 11a and b displays the LCI findings of the Japan coast that was affected by the East China Sea oil spill where the leaf chlorophyll area was 197 km² before the oil spill but after the event, the total leaf chlorophyll area declined by 18 km² as shown in Figs 11c and d. The LCI analysis of the Balikpapan Bay region reveals significant changes in the chlorophyll content of the area. Figures 11e and f displays the area with leaf chlorophyll was 238 km² before the incident. Figure 11g displays the LCI results for 31 August 2018 five months after the event, indicating a reduction of

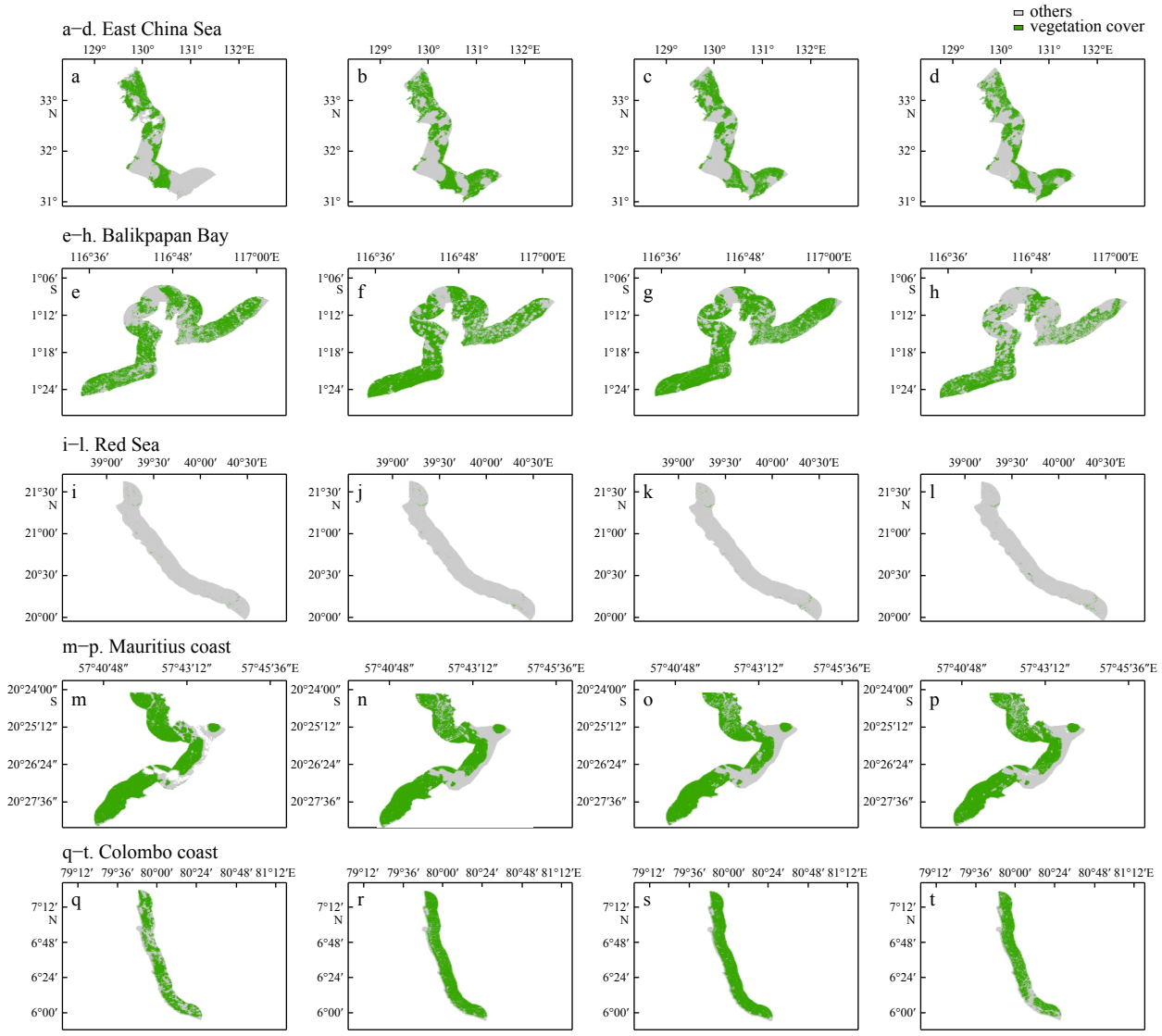

Fig. 9. NDVI based assessment for oil spill impacts: time-series NDVI maps showing vegetation changes in the coastal regions affected by oil spills. Subplots: a. East China Sea (2016-05-05), b. East China Sea (2017-10-09), c. East China Sea (2018-10-09), d. East China Sea (2019-10-09), e. Balikpapan Bay (2016-08-07), f. Balikpapan Bay (2017-08-31), g. Balikpapan Bay (2018-08-31), h. Balikpapan Bay (2019-08-31), i. Red Sea Jeddah (2017-03-23), j. Red Sea Jeddah (2018-03-23), k. Red Sea Jeddah (2020-03-22), l. Red Sea Jeddah (2021-03-22), m. Mauritius (2018-01-29), n. Mauritius (2019-01-29), o. Mauritius (2021-01-28), p. Mauritius (2022-01-28), q. Colombo (2019-11-17), r. Colombo (2020-11-21), s. Colombo (2021-11-21), t. Colombo (2022-11-26).

leaf chlorophyll from 238 km^2 to 196 km^2. The findings suggest that areas with leaf chlorophyll decreased by 79 km^2 in each successive year. The LCI findings of the Jeddah coast didn't show any significant changes in the leaf chlorophyll area because the vegetation covered area was not enough to detect the impacts as shown in Figs 11i and l.

The LCI findings of the Mauritius coast depicted the variations in leaf chlorophyll area. Approximately the area of leaf chlorophyll was 50 km^2 as shown in Figs 11m and n, however, two years after the event, the leaf chlorophyll area reduced from 50 km^2 to 28 km^2 as shown in Figs 11o and p. Figure 11q displays the LCI findings of the Colombo coast where the area of leaf chlorophyll before the two years of the event was 60 km^2 but in the years later the area of LCI increased sharply up to 73 km^2 to 78 km^2 respectively as shown in Fig. 11r. However, two years after the event, the chlorophyll area dropped significantly to 43 km^2 as shown in Figs 11s and t.

4.4.4 *NDWI based assessment*

The NDWI technique was applied to assess the effects on the water content of the leaves. Figure 12a displays the area of water within leaves was 405 km^2 before the oil spill on 5 May 2016. Figure 12b displays that the water area within the leaves diminished up to 410 km^2 before the one year of oil spill. Figures 12c and d displays the reduction of the water area within leaves of the coastal region. The NDWI analysis of the Balikpapan Bay oil spill did not reveal any type of impact before the event as shown in Fig. 12e, where the water area within the leaves was 117 km^2. However, after the oil spill, the effects became more and more severe in each successive year and water area within leaves reduced to 80 km^2 as shown in Figs 12g and h. Findings of NDWI over the coast of Jeddah show few variations because the area of vegetation was not enough to monitor the impacts as shown in Figs 12i–l. The NDWI findings of the Mauritius coast indicate that the area of water within the leaves before the oil spill was 27 km^2

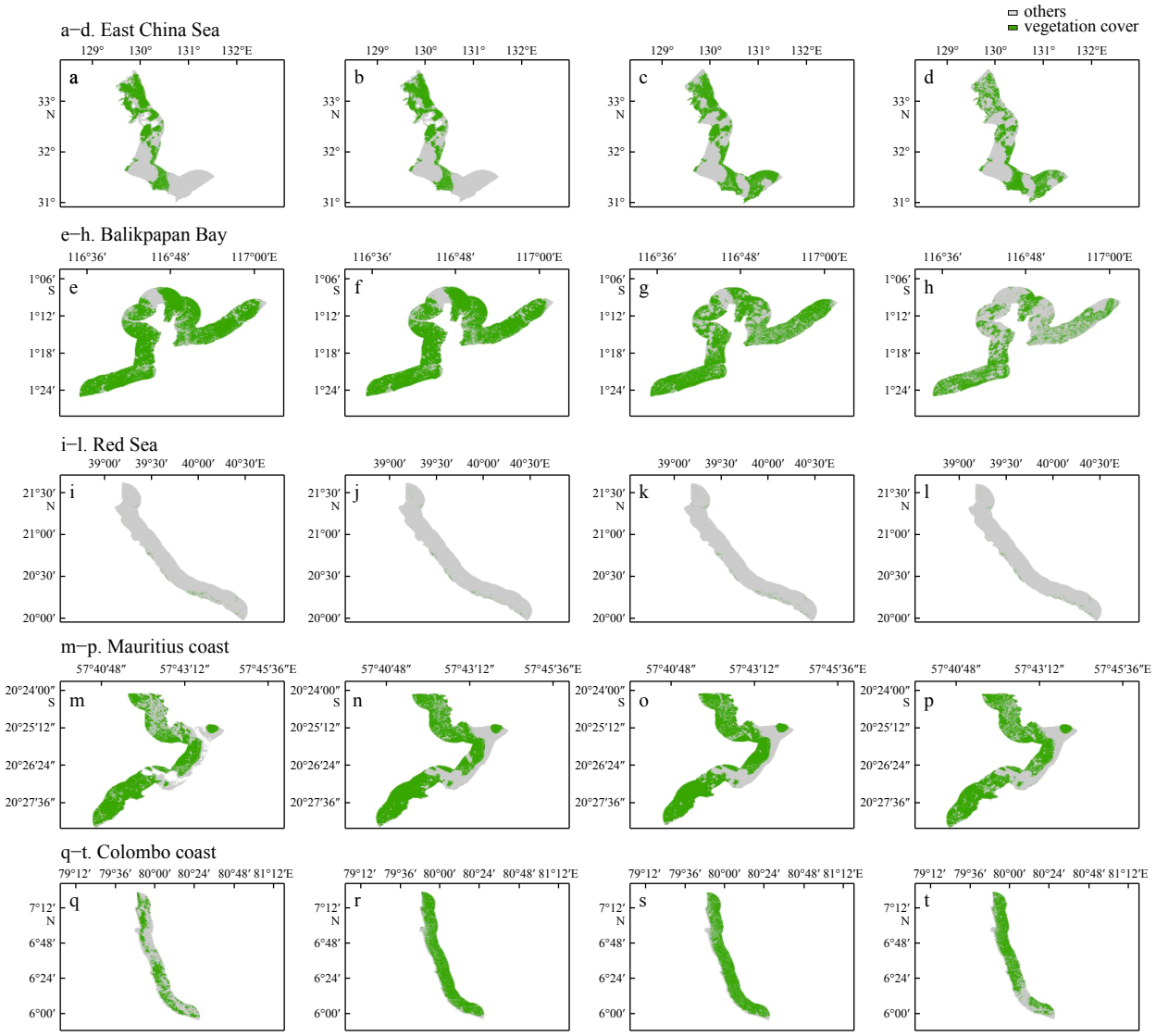

Fig. 10. EVI based assessment for oil spill impacts: time-series EVI maps showing vegetation health in the coastal regions affected by oil spills. Subplots: a. East China Sea (2016-05-05), b. East China Sea (2017-10-09), c. East China Sea (2018-10-09), d. East China Sea (2019-10-09), e. Balikpapan Bay (2016-08-07), f. Balikpapan Bay (2017-08-31), g. Balikpapan Bay (2018-08-31), h. Balikpapan Bay (2019-08-31), i. Red Sea Jeddah (2017-03-23), j. Red Sea Jeddah (2018-03-23), k. Red Sea Jeddah (2020-03-22), l. Red Sea Jeddah (2021-03-22), m. Mauritius (2018-01-29), n. Mauritius (2019-01-29), o. Mauritius (2021-01-28), p. Mauritius (2022-01-28), q. Colombo (2019-11-17), r. Colombo (2020-11-21), s. Colombo (2021-11-21), t. Colombo (2022-11-26).

and 42 km^2. The spatial visualization of these findings as shown in Figs 12m and n but after the event the water area within leaves reduced up to 16 km^2 as shown in Figs 12o and p. The NDWI findings over the coast of Colombo show that the area of water within leaves in the two years before the event was the same, which is 18 km^2 but the abrupt increase of 24 km^2 was seen one year before the event. However, after two years of the event a significant decline as shown in Figs 12s and t.

4.5 *Air Quality Impact assessment*

Oil spill impacts are not only limited to marine life and coastal vegetation but also affect the quality of air. When oil spills catch fire, it releases many harmful gasses into the atmosphere. Some of the toxic gases released from the burning of the oil spill are CO, NO_2, SO_2, and various organic compounds. Based on the availability of data, two oil spill events including Sri Lanka and the Red Sea were selected for air quality assessment using S-5P satellite data (Zheng et al., 2019). Figure 13 displays the concentration of air pollutants over the Red Sea. Post event, CO concentration is observed 0.028 mol/m^2 as shown in Fig. 13a whereas, after the event, its concentration increased to 0.031 mol/m^2. Figure 13b displays the mean concentration of NO_2 one-month pre- and post-event. The level of NO_2 was 0.000 049 mol/m^2 one month before the event but after the burning of crude oil, concentration was observed 0.000 054 359 mol/m^2. Figure 13c displays the concentration of SO_2 was 0.000 131 5 mol/m^2 one month before the event but after the event, its concentration increased up to 0.000 28 mol/m^2. Figure 14 displays the effects of oil combustion on the air quality of Colombo. Figure 14a displays the CO concentration was 0.023 425 mol/m^2 before the event, however, concentration was increased to 0.034 9 mol/m^2 after the event. Figure 14b displays the concentration of NO_2 was 0.000 044 8 mol/m^2 before the event, however, concentration was increased to 0.000 05 mol/m^2 after the incident. Figure 14c displays the mean

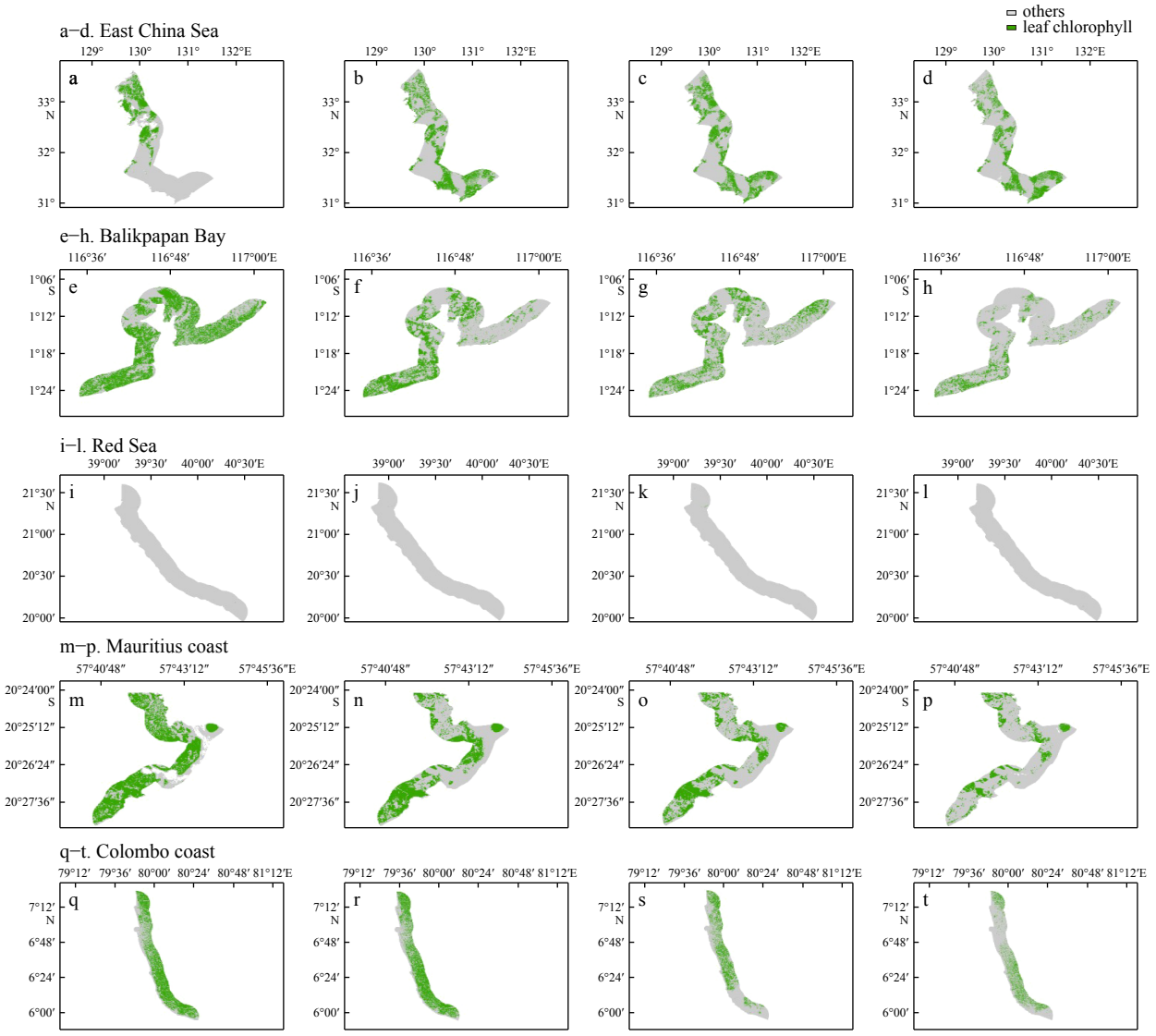

Fig. 11. LCI based assessment for oil spill impacts: time-series LCI maps showing chlorophyll content in the vegetation of the coastal regions affected by oil spills. Subplots: a. East China Sea (2016-05-05), b. East China Sea (2017-10-09), c. East China Sea (2018-10-09), d. East China Sea (2019-10-09), e. Balikpapan Bay (2016-08-07), f. Balikpapan Bay (2017-08-31), g. Balikpapan Bay (2018-08-31), h. Balikpapan Bay (2019-08-31), i. Red Sea Jeddah (2017-03-23), j. Red Sea Jeddah (2018-03-23), k. Red Sea Jeddah (2020-03-22), l. Red Sea Jeddah (2021-03-22), m. Mauritius (2018-01-29), n. Mauritius (2019-01-29), o. Mauritius (2021-01-28), p. Mauritius (2022-01-28), q. Colombo (2019-11-17), r. Colombo (2020-11-21), s. Colombo (2021-11-21), t. Colombo (2022-11-26).

concentration of SO_2 in the coastal area of Colombo and its concentration was 0.044 4 mol/m^2 before the incident, however, concentration was increased up to 0.186 mol/m^2 after the event.

5 Discussion

SAR-based techniques have proven effective for detecting marine oil spills and evaluating consequences on the surroundings because of such incidents. SAR data can capture high resolution images of ocean surface in all weather conditions making this technique highly effective (Fingas and Brown, 2014). In this study, S-1, S-2, and S-5P satellite datasets were utilized to identify oil spills in five locations such as the East China Sea, Balikpapan Bay, Red Sea, Mauritius coast, and Colombo coast. The S-1 data can successfully distinguish between clean sea and oil slicks, but false positives due to natural phenomena like algae blooms are a concern. The S-2 provides multispectral satellite data, which was utilized for assessing the effects of oil spills on coastal vegetation, though cloud cover often obstructs clear observations. The S-5P data was used to study the effects of toxic gases on air pollution produced by burning crude oil, although calibration errors can affect accuracy (Veefkind et al., 2012).

Huete et al. (2002) emphasized that after an oil spill incident NDVI and EVI techniques can be utilized to estimate the amount of damage to coastal vegetation. Also, in case that crude oil catches fire, the release of hazardous gases as a result damages the air quality (Eskes et al., 2015). The impact of oil spills on the environment and human health cannot be overstated, particularly when it comes to plant life in coastal regions. The Balikpapan Bay oil spill is a prime example of how significant vegetation loss can occur over a considerable area measuring roughly 118 km^2. Plant systems are severely compromised by an oil spill's aftermath, as they are covered by crude oil which reduces their capacity for photosynthesis and nutrient absorption (Lin and Mendelssohn, 2012). In consequence, plants may become unpro-

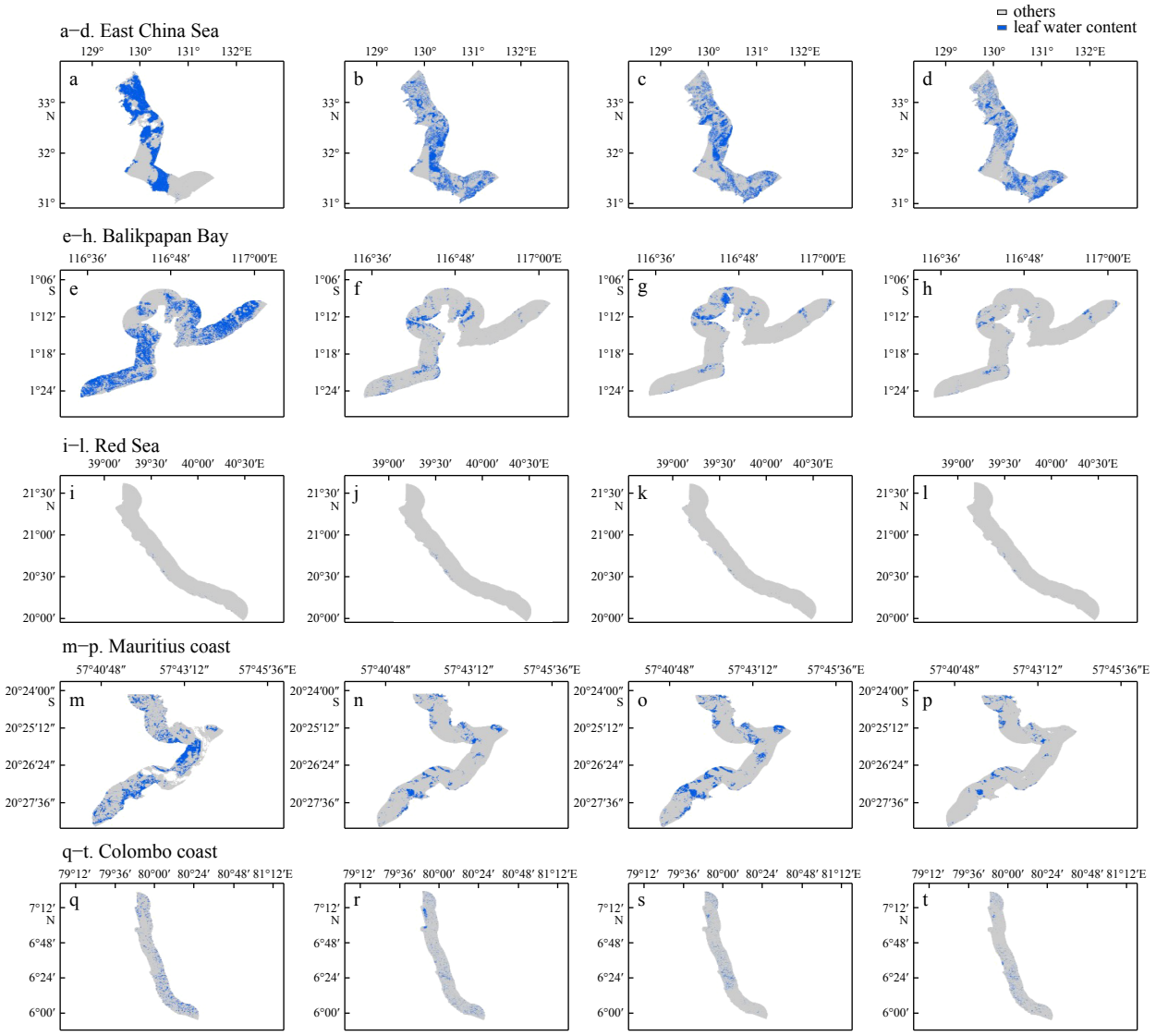

Fig. 12. NDWI based assessment for oil spill impacts: time-series NDWI maps highlighting changes in water presence and potential oil contamination in the coastal regions. Subplots: a. East China Sea (2016-05-05), b. East China Sea (2017-10-09), c. East China Sea (2018-10-09), d. East China Sea (2019-10-09), e. Balikpapan Bay (2016-08-07), f. Balikpapan Bay (2017-08-31), g. Balikpapan Bay (2018-08-31), h. Balikpapan Bay (2019-08-31), i. Red Sea Jeddah (2017-03-23), j. Red Sea Jeddah (2018-03-23), k. Red Sea Jeddah (2020-03-22), l. Red Sea Jeddah (2021-03-22), m. Mauritius (2018-01-29), n. Mauritius (2019-01-29), o. Mauritius (2021-01-28), p. Mauritius (2022-01-28), q. Colombo (2019-11-17), r. Colombo (2020-11-21), s. Colombo (2021-11-21), t. Colombo (2022-11-26).

ductive, causing them to lose their natural wildlife surroundings and leading to elevated erosion in the affected sites (Peterson et al., 2003a).

Oil spills can severely damage the environment, ecosystems, coastal vegetation, and air quality. Spills can have long lasting consequences that can persist for years causing large term damage to the environment and organisms that live there (Peterson et al., 2003a, b). Wind direction has impacts on oil spill movement as it generates ocean currents on the surface that dragged oil at the wind and currents direction. However, rapid changes in wind patterns can lead to unpredictable spill trajectories, complicating cleanup efforts. Along with that wind speed also has a great impact on the accuracy of oil spill detection. Wind speed between 1.5 m/s to 9 m/s is perfect for the detection of oil spill in this study wind speed for all the events was between 1.5 m/s to 9 m/s. Therefore, oil spills were detected successfully.

The environment and human health can face detrimental effects from the release of toxic gases such as CO, NO_2, and SO_2 during an oil spill incident, making air quality one of the major concerns. Inhalation of these gases could result in several problems such as eye irritation, skin irritation, and respiratory illnesses. Furthermore, their presence contributes to the formation of ground-level ozone and acid rain. Sri Lanka and Red Sea events were analyzed using S-5P NRT data to determine the concentration levels of hazardous fumes. As Lehr et al. (1984) study, due to low vegetation cover in the vicinity of the Red Sea oil spill, its impact on its impact on vegetation cover was considerably limited but its impacts on the air quality are high. To effectively mitigate environmental hazards and human health risks, scientists should continuously measure and assess the impacts of such events on both vegetation cover and air quality.

6 Summary and conclusions

In this study, five reported oil spills incidents were detected

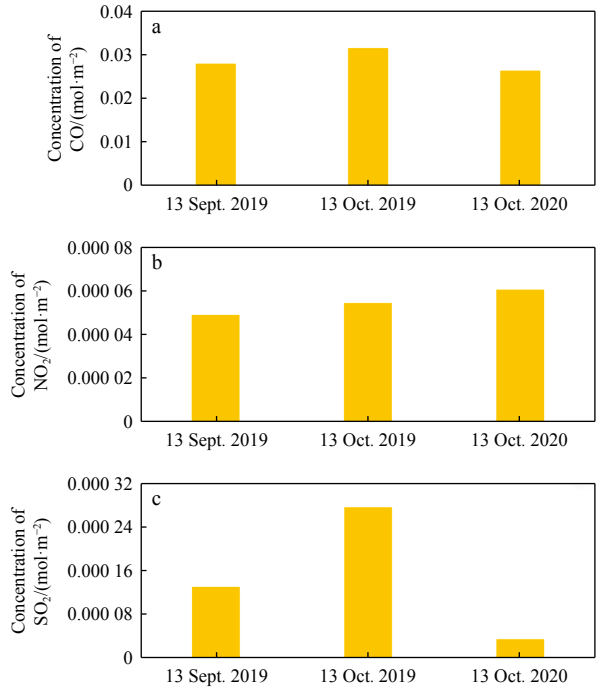

Fig. 13. Air quality impact assessment of the Red Sea oil spill: a. temporal variation in concentration of carbon monoxide (CO) levels, b. changes in the mean concentration of nitrogen dioxide (NO_2), and c. concentration of sulfur dioxide (SO_2).

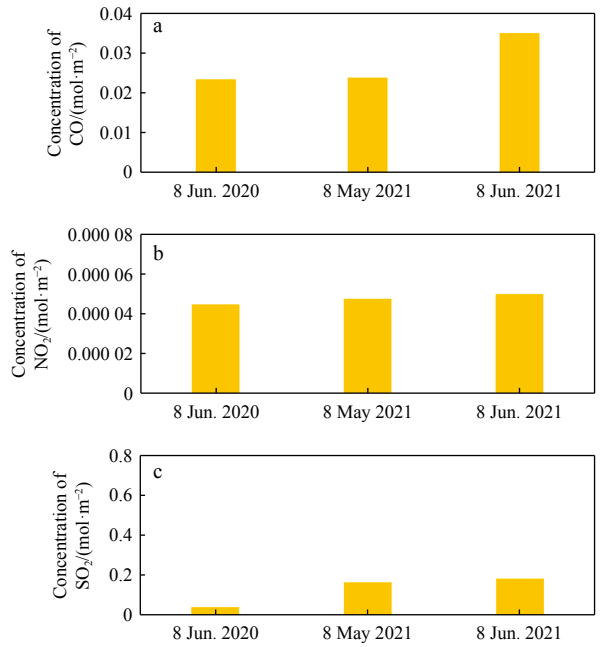

Fig. 14. Air quality impact assessment of the Sri Lanka oil spill: a. temporal variation in concentration of carbon monoxide (CO) levels, b. changes in the mean concentration of nitrogen dioxide (NO_2), and c. concentration of sulfur dioxide (SO_2).

successfully using active RS techniques, along with that impacts of oil spills on vegetation cover and air quality were also analyzed using optical RS technique. SAR-based oil spill detection techniques were proven cost effective for mapping and monitoring of oil spills at ocean surface. Oil has a disastrous effect on the fragile marine ecosystem. Therefore, impacts of oil spill on vegetation cover were assessed using different vegetation indices such as NDVI, EVI, LCI, and NDWI. Furthermore, the impact of oil spills on the air quality is also monitored. It is concluded as follows.

Wind speed in the East China Sea during the oil spill event was high and made the detection process quite difficult. Two slicks of 52 km^2 were reported but due to high wind speed, only a small patch of oil slick was detected. The movement of oil was towards the coastal areas of Japan and South Korea. Area around 10 km^2 computed using NDVI, 29 km^2 computed using EVI, 18 km^2 computed using LCI was affected by the oil spill.

The Balikpapan oil spill was detected successfully and a total of 4 648 × 4 587 pixels were analyzed, and there were no look-alikes in the image. This spill affected 510 km^2 vegetation cover of the surrounding area.

The Red Sea oil spill was a massive oil spill that polluted around 1 300 km^2 area. A total of 8 911×8 221 pixels were processed with a threshold value of less than –4.5 dB to detect the spilled oil. After the spill, concentrations of CO, NO_2, SO_2 was observed 0.031 mol/m^2, 20.000 054 359 mol/m^2, and 0.000 28 mol/m^2, respectively.

Mauritius coastal area is very sensitive and a habitat of rare species. A total of 501 × 352 pixels were processed to accomplish the purpose of oil spill detection. After the event the water area within leaves reduced up to 16 km^2.

Feature extraction techniques were applied to detect the oil spill of Sri Lanka, near the coast of Colombo, because of the presence of look-alikes in the SAR imagery. The Sri Lanka oil spill has not only affected the vegetation area but also degraded the quality of surrounding air because of crude oil combustion. After the oil spill, approximately 24 km^2 vegetation covered area was affected, whereas concentrations of CO, NO_2, and SO_2 were observed as 0.034 9 mol/m^2, 0.000 05 mol/m^2, and 0.186 mol/m^2 respectively.

Wind speed and direction were also plotted for all the events via wind-rose diagram, and it is concluded that wind speed ranging from 3 m/s to 9 m/s are favorable for the oil spill detection. It was also observed that that wind direction significantly impacts oil spill movement.

Validation of numerical models that forecast oil spill trajectories are suggested to be used for mapping the geographical distribution of an oil spill. To further enhance the quality of the output, machine learning and deep learning-based techniques such as artificial neural networks, fractal dimensions, fuzzy logic, and completely polarized SAR imaging can be employed. Additionally, RS methods such as VI can be used to identify and track vegetation in mangrove forests that have been impacted by oil spills, allowing for early mitigation responses to lessen the environmental impact.

Acknowledgements

The authors would like to thank COMSATS University Islamabad (CUI) for providing excellent research facilities to support this work. They also extend their gratitude to Scientific Data Hub for providing Sentinel-1 data.

References

Adamu B, Tansey K, Ogutu B. 2018. Remote sensing for detection and monitoring of vegetation affected by oil spills. International Journal of Remote Sensing, 39(11): 3628–3645, doi: 10.1080/01431161.2018.1448483

Ajadi O A, Meyer F J, Tello M, et al. 2018. Oil spill detection in synthetic aperture radar images using Lipschitz-regularity and

multiscale techniques. IEEE Journal of Selected Topics in Applied Earth Observations and Remote Sensing, 11(7): 2389–2405, doi: 10.1109/JSTARS.2018.2827996

Alaa El-Din G, Amer A A, Malsh G, et al. 2018. Study on the use of banana peels for oil spill removal. Alexandria Engineering Journal, 57(3): 2061–2068, doi: 10.1016/j.aej.2017.05.020

Alpers W, Holt B, Zeng Kan. 2017. Oil spill detection by imaging radars: challenges and pitfalls. Remote Sensing of Environment, 201: 133–147, doi: 10.1016/j.rse.2017.09.002

Arellano P, Tansey K, Balzter H, et al. 2015. Detecting the effects of hydrocarbon pollution in the Amazon forest using hyperspectral satellite images. Environmental Pollution, 205: 225–239, doi: 10.1016/j.envpol.2015.05.041

Bhatnagar S, Gill L, Regan S, et al. 2020. Mapping vegetation communities inside wetlands using Sentinel-2 imagery in Ireland. International Journal of Applied Earth Observation and Geoinformation, 88: 102083, doi: 10.1016/j.jag.2020.102083

Brekke C, Solberg A H S. 2005. Oil spill detection by satellite remote sensing. Remote Sensing of Environment, 95(1): 1–13, doi: 10.1016/j.rse.2004.11.015

Cantorna D, Dafonte C, Iglesias A, et al. 2019. Oil spill segmentation in SAR images using convolutional neural networks. A comparative analysis with clustering and logistic regression algorithms. Applied Soft Computing, 84: 105716, doi: 10.1016/j.asoc.2019.105716

Cervantes-Hernández P, Celis-Hernández O, Ahumada-Sempoal M A, et al. 2024. Combined use of SAR images and numerical simulations to identify the source and trajectories of oil spills in coastal environments. Marine Pollution Bulletin, 199: 115981, doi: 10.1016/j.marpolbul.2023.115981

Chiu C M, Huang Ching-Jer, Wu Li-Chung, et al. 2018. Forecasting of oil-spill trajectories by using SCHISM and X-band radar. Marine Pollution Bulletin, 137: 566–581, doi: 10.1016/j.marpolbul.2018.10.060

Clevers J G P W, Gitelson A A. 2013. Remote estimation of crop and grass chlorophyll and nitrogen content using red-edge bands on Sentinel-2 and -3. International Journal of Applied Earth Observation and Geoinformation, 23: 344–351, doi: 10.1016/j.jag.2012.10.008

Delegido J, Verrelst J, Alonso L, et al. 2011. Evaluation of Sentinel-2 red-edge bands for empirical estimation of green LAI and chlorophyll content. Sensors, 11(7): 7063–7081, doi: 10.3390/s110707063

Drusch M, Del Bello U, Carlier S, et al. 2012. Sentinel-2: ESA's optical high-resolution mission for GMES operational services. Remote Sensing of Environment, 120: 25–36, doi: 10.1016/j.rse.2011.11.026

Eskes H, Huijnen V, Arola A, et al. 2015. Validation of reactive gases and aerosols in the MACC global analysis and forecast system. Geoscientific Model Development, 8(11): 3523–3543, doi: 10.5194/gmd-8-3523-2015

Evans D D, Mulholland G W, Baum H R, et al. 2001. *In situ* burning of oil spills. Journal of Research of the National Institute of Standards and Technology, 106(1): 231–278, doi: 10.6028/jres.106.009

Ewing B R, Hawkins T R, Wiedmann T O, et al. 2012. Integrating ecological and water footprint accounting in a multi-regional input-output framework. Ecological Indicators, 23: 1–8, doi: 10.1016/j.ecolind.2012.02.025

Fan Jianchao, Zhang Fengshou, Zhao Dongzhi, et al. 2015. Oil spill monitoring based on SAR remote sensing imagery. Aquatic Procedia, 3: 112–118, doi: 10.1016/j.aqpro.2015.02.234

Fingas M, Brown C. 2014. Review of oil spill remote sensing. Marine Pollution Bulletin, 83(1): 9–23, doi: 10.1016/j.marpolbul.2014.03.059

Fingas M, Brown C E. 2018. A review of oil spill remote sensing. Sensors, 18(1): 91

Fiscella B, Giancaspro A, Nirchio F, et al. 2000. Oil spill detection using marine SAR images. International Journal of Remote Sensing, 21(18): 3561–3566, doi: 10.1080/014311600750037589

Frampton W J, Dash J, Watmough G, et al. 2013. Evaluating the capabilities of Sentinel-2 for quantitative estimation of biophysical variables in vegetation. ISPRS Journal of Photogrammetry and Remote Sensing, 82: 83–92, doi: 10.1016/j.isprsjprs.2013.04.007

Freedman B. 1995. The ecological effects of pollution, disturbance, and other stresses. In: Freedman B, ed. Environmental Ecology. 2nd ed. Amsterdam: Elsevier, 1–10

Ganjirad M, Bagheri H. 2024. Google Earth Engine-based mapping of land use and land cover for weather forecast models using Landsat 8 imagery. Ecological Informatics, 80: 102498, doi: 10.1016/j.ecoinf.2024.102498

Guanter L, Aben I, Tol P, et al. 2015. Potential of the TROPOspheric Monitoring Instrument (TROPOMI) onboard the Sentinel-5 Precursor for the monitoring of terrestrial chlorophyll fluorescence. Atmospheric Measurement Techniques, 8(3): 1337–1352, doi: 10.5194/amt-8-1337-2015

Huete A, Didan K, Miura T, et al. 2002. Overview of the radiometric and biophysical performance of the MODIS vegetation indices. Remote Sensing of Environment, 83(1/2): 195–213, doi: 10.1016/S0034-4257(02)00096-2

Jana A, Maiti S, Biswas A. 2016. Seasonal change monitoring and mapping of coastal vegetation types along Midnapur-Balasore coast, Bay of Bengal using multi-temporal Landsat data. Modeling Earth Systems and Environment, 2(1): 7, doi: 10.1007/s40808-015-0062-x

Khanna S, Santos M J, Ustin S L, et al. 2013. Detection of salt marsh vegetation stress and recovery after the deepwater horizon oil spill in Barataria Bay, Gulf of Mexico using AVIRIS data. PLoS One, 8(11): e78989, doi: 10.1371/journal.pone.0078989

Lee J S, Wen J H, Ainsworth T L, et al. 2008. Improved sigma filter for speckle filtering of SAR imagery. IEEE Transactions on Geoscience and Remote Sensing, 47: 202–213

Lehr W J, Fraga R J, Belen M S, et al. 1984. A new technique to estimate initial spill size using a modified Fay-type spreading formula. Marine Pollution Bulletin, 15(9): 326–329, doi: 10.1016/0025-326X(84)90488-0

Li Lin, Ustin S L, Lay M. 2005. Application of AVIRIS data in detection of oil-induced vegetation stress and cover change at Jornada, New Mexico. Remote Sensing of Environment, 94(1): 1–16, doi: 10.1016/j.rse.2004.08.010

Lin Qianxin, Mendelssohn I A. 2012. Impacts and recovery of the *Deepwater horizon* oil spill on vegetation structure and function of coastal salt marshes in the northern gulf of Mexico. Environmental Science & Technology, 46(7): 3737–3743

Lu Jiang. 2003. Marine oil spill detection, statistics and mapping with ERS SAR imagery in south-east Asia. International Journal of Remote Sensing, 24(15): 3013–3032, doi: 10.1080/01431160110076216

Mahindapala W K M. 2020. Oil spill detection in the east of Sri Lanka with Sentinel-1 SAR. E3S Web of Conferences, 211: 02013, doi: 10.1051/e3sconf/202021102013

Malenovský Z, Rott H, Cihlar J, et al. 2012. Sentinels for science: potential of Sentinel-1, -2, and -3 missions for scientific observations of ocean, cryosphere, and land. Remote Sensing of Environment, 120: 91–101, doi: 10.1016/j.rse.2011.09.026

Marghany M, Van Genderen J. 2014. Entropy algorithm for automatic detection of oil spill from radarsat-2 SAR data. IOP Conference Series: Earth and Environmental Science, 18: 012051, doi: 10.1088/1755-1315/18/1/012051

Mdakane L W, Kleynhans W. 2022. Feature selection and classification of oil spill from vessels using Sentinel-1 wide–swath synthetic aperture radar data. IEEE Geoscience and Remote Sensing Letters, 19: 4002505

Mera D, Cotos J M, Varela-Pet J, et al. 2012. Adaptive thresholding algorithm based on SAR images and wind data to segment oil spills along the northwest coast of the Iberian Peninsula. Marine Pollution Bulletin, 64(10): 2090–2096, doi: 10.1016/j.marpolbul.2012.07.018

Migliaccio M, Nunziata F, Buono A. 2015. SAR polarimetry for sea oil slick observation. International Journal of Remote Sensing, 36(12): 3243–3273, doi: 10.1080/01431161.2015.1057301

Misra A, Balaji R. 2017. Simple approaches to oil spill detection using sentinel application platform (SNAP)-ocean application

tools and texture analysis: a comparative study. Journal of the Indian Society of Remote Sensing, 45(6): 1065–1075, doi: 10.1007/s12524-016-0658-2

Naz S, Iqbal M F, Mahmood I, et al. 2021. Marine oil spill detection using synthetic aperture radar over Indian Ocean. Marine Pollution Bulletin, 162: 111921, doi: 10.1016/j.marpolbul.2020.111921

Noomen M F, Skidmore A K. 2009. The effects of high soil CO_2 concentrations on leaf reflectance of maize plants. International Journal of Remote Sensing, 30(2): 481–497, doi: 10.1080/01431160802339431

Nukapothula S, Wu Jie, Chen Chuqun, et al. 2021. Potential impact of the extensive oil spill on primary productivity in the Red Sea waters. Continental Shelf Research, 222: 104437, doi: 10.1016/j.csr.2021.104437

Nur A A, Mandang I, Mubarrok S, et al. 2018. The changes of water mass characteristics using 3-dimensional Regional Ocean Modeling System (ROMS) in Balikpapan bay, Indonesia. IOP Conference Series: Earth and Environmental Science, 162: 012006, doi: 10.1088/1755-1315/162/1/012006

Ozigis M S, Kaduk J D, Jarvis C H, et al. 2020. Detection of oil pollution impacts on vegetation using multifrequency SAR, multispectral images with fuzzy forest and random forest methods. Environmental Pollution, 256: 113360, doi: 10.1016/j.envpol.2019.113360

Peng Wenfu, Kuang Tingting, Tao Shuai. 2019. Quantifying influences of natural factors on vegetation NDVI changes based on geographical detector in Sichuan, western China. Journal of Cleaner Production, 233: 353–367, doi: 10.1016/j.jclepro.2019.05.355

Peng Wenfu, Wang Guangjie, Zhou Jieming, et al. 2016. Dynamic monitoring of fractional vegetation cover along Minjiang River from Wenchuan County to Dujiangyan City using multi-temporal Landsat 5 and 8 images. Acta Ecologica Sinica, 36(7): 1975–1988

Peterson G D, Carpenter S R, Brock W A. 2003a. Uncertainty and the management of multistate ecosystems: an apparently rational route to collapse. Ecology, 84(6): 1403–1411, doi: 10.1890/0012-9658(2003)084[1403:UATMOM]2.0.CO;2

Peterson C H, Rice S D, Short J W, et al. 2003b. Long-term ecosystem response to the Exxon Valdez oil spill. Science, 302(5653): 2082–2086, doi: 10.1126/science.1084282

Prastyani R, Basith A. 2018. Utilisation of Sentinel-1 SAR imagery for oil spill mapping: a case study of Balikpapan Bay oil spill. Journal of Geospatial Information Science and Engineering, 1(1): 22–26

Pu Ruiliang, Gong Peng, Yu Qian. 2008. Comparative analysis of EO-1 ALI and Hyperion, and Landsat ETM+ data for mapping forest crown closure and leaf area index. Sensors, 8(6): 3744–3766, doi: 10.3390/s8063744

Rajendran S, Vethamony P, Sadooni F N, et al. 2021. Detection of wakashio oil spill off Mauritius using Sentinel-1 and 2 data: capability of sensors, image transformation methods and mapping. Environmental Pollution, 274: 116618, doi: 10.1016/j.envpol.2021.116618

Schlemmer M, Gitelson A, Schepers J, et al. 2013. Remote estimation of nitrogen and chlorophyll contents in maize at leaf and canopy levels. International Journal of Applied Earth Observation and Geoinformation, 25: 47–54, doi: 10.1016/j.jag.2013.04.003

Shu Y, Li J, Yousif H, et al. 2010. Dark-spot detection from SAR intensity imagery with spatial density thresholding for oil-spill monitoring. Remote Sensing of Environment, 114: 2026–2035, doi: 10.1016/j.rse.2010.04.009

Skrunes S, Brekke C, Eltoft T. 2014. Characterization of marine surface slicks by Radarsat-2 multipolarization features. IEEE Transactions on Geoscience and Remote Sensing, 52(9): 5302–5319, doi: 10.1109/TGRS.2013.2287916

Somvanshi S S, Kumari M. 2020. Comparative analysis of different vegetation indices with respect to atmospheric particulate pollution using sentinel data. Applied Computing and Geosciences, 7: 100032, doi: 10.1016/j.acags.2020.100032

Topouzelis K, Singha S. 2017. Oil spill detection using space-borne sentinel-1 SAR imagery. In: Fingas M, ed. Oil Spill Science and Technology. 2nd ed. Amsterdam: Elsevier, 387–402

Vankayalapati K, Dasari H P, Langodan S, et al. 2023. Multi-mission satellite detection and tracking of October 2019 Sabiti oil spill in the Red Sea. Remote Sensing, 15(1): 38

Veefkind J P, Aben I, McMullan K, et al. 2012. TROPOMI on the ESA Sentinel-5 precursor: A GMES mission for global observations of the atmospheric composition for climate, air quality and ozone layer applications. Remote Sensing of Environment, 120: 70–83, doi: 10.1016/j.rse.2011.09.027

Yekeen S T, Balogun A L, Yusof K B W. 2020. A novel deep learning instance segmentation model for automated marine oil spill detection. ISPRS Journal of Photogrammetry and Remote Sensing, 167: 190–200, doi: 10.1016/j.isprsjprs.2020.07.011

Yin Liping, Zhang Min, Zhang Yuanling, et al. 2018. The long-term prediction of the oil-contaminated water from the *Sanchi* collision in the East China Sea. Acta Oceanologica Sinica, 37(3): 69–72, doi: 10.1007/s13131-018-1193-5

Zalik K R 2008. An efficient K-means clustering algorithm. Pattern Recognition Letters, 29, 1385–1391

Zhang Mei, Sun Xian, Xu Jilin. 2020. Heavy metal pollution in the East China Sea: a review. Marine Pollution Bulletin, 159: 111473, doi: 10.1016/j.marpolbul.2020.111473

Zhao Jun, Temimi M, Al Azhar M, et al. 2015. Satellite-based tracking of oil pollution in the Arabian Gulf and the sea of Oman. Canadian Journal of Remote Sensing, 41(2): 113–125, doi: 10.1080/07038992.2015.1042543

Zheng Zihao, Yang Zhiwei, Wu Zhifeng, et al. 2019. Spatial variation of NO_2 and its impact factors in China: an application of Sentinel-5P products. Remote Sensing, 11(16): 1939, doi: 10.3390/rs11161939